Study of Belleville Springs and Bond Graph Analysis
of
Passive Vibration Assisted Rotary Drilling Tool

by

Dipesh Maharjan

A thesis submitted to the School of Graduate Studies in partial fulfillment of the requirements for the degree of

Master of Engineering

Department of Engineering and Applied Science

Memorial University of Newfoundland

St. John's, NL, CA

October 2020

Abstract

Since 2008, the effect of active/passive sources of drilling vibration has been a topic of research at the Drilling Technology Laboratory of Memorial University of Newfoundland. Drill-off tests have been conducted in many different settings using fully instrumented lab-scale drill rigs (Small Drilling Simulator (SDS) and Large Drilling Simulator (LDS)) and through field trials in order to validate these effects and the researchers have been able to acquire substantially prominent results, which is evident from improved drilling rates and increased dynamic downhole weight on bit (DDWOB). One of the outcomes from those experiments is the development of novel passive Vibration assisted Rotary Drilling (p-VARD) Tool, which harnesses the vibration generated at bit-rock interface to improve the drilling rate and the measured DDWOB. The p-VARD tool uses different configuration of Belleville springs and elastomer to produce desired value of tool compliance and modify the damping. The research outcomes in this thesis explain the dynamic behaviour of the p-VARD tool and helps us understand the actual phenomenon inside the tool, which results in this behaviour. Mass-spring-damper schematics of the rigid and compliant drilling systems are analyzed with the help of bond graphs in 20-sim. Results show that the p-VARD can lower the drill string natural frequency significantly enabling it to resonate at the frequencies of the top drive.

In order to facilitate the p-VARD experiments in a more controlled environment, the tool has been designed for the LDS, which is more advanced than the SDS. The dynamic simulation of the Belleville springs is in itself, a separate area of research that is used for the dynamic analysis of the p-VARD tool design. The LDS offers a wide range of rotary speeds and weight on bit and can be operated fully automatically or manually. P-VARD experiments in LDS will enable us to

characterize the tool properties in more depth. The LDS p-VARD tool is designed with a minimum safety factor of 3.4 against the maximum torque generated by the LDS. It utilizes a uniformly grooved sensor plates with five identical and one distinct cross-section, which is attached to the outer shell to track the axial movement of the tool. The tool is designed such that the torque is transmitted from the inner shaft to the outer shell through four uniformly spaced keys and for fluid transmission, a 13 mm through hole is made through the middle of the tool.

Acknowledgements

I would like to thank Prof. Stephen Butt for his expert guidance and supervision throughout my Masters program. Also, I would like to thank Prof. Geoff Rideout for his help and support in my research works. The researches in this thesis would not have been possible without the collaboration of the members of the Drilling Technology Laboratory, my special thanks to the DTL Lab Manager, Dr. Abdelsalam Abugharara, Sustainable Mining by Drilling Project Manager, Jeronimo de Moura Junior and all the DTL members. I would also like to thank Dr. Mohammed Taleb-Berrouane, R & D Project Manager at C-RISE for his constant guidance and support.

I would like to dedicate this thesis to all the members of my family; father, Krishna Gopal, mother, Bardi Maya, sisters Lina and Anika, brother, Ashesh and my beloved Wife, Manju (Manna).

Table of Contents

List of Figures

List of Tables

List of Symbols, Nomenclature/Abbreviations

Symbols/Abbreviations related to Belleville springs

t	Spring thickness
r_1	Spring inner radius
r_2	Spring outer radius
γ	Diameter ratio
h	Spring free height
H	Spring total height
$\emptyset$	Spring angle
θ	Angle of neutral line
δ	Spring deflection
P	Spring load
E	Young's Modulus
ϑ	Poisson's ratio
I	Number of springs in series
J	Number of springs in parallel
u_e	Edge displacement
u_s	Surface displacement
μ_e	Edge friction factor
μ_s	Surface friction factor

Symbols/Abbreviations related to p-VARD and drilling

p-VARD   Passive Vibration Assisted Rotary Drilling

b   Damping coefficient

ζ Damping ratio

ROP   Rate of Penetration

WOB   Weight On Bit

DDWOB   Dynamic Downhole Weight On Bit

TOB   Torque On Bit

PDC   Polycrystalline Diamond Compact

MSE   Mechanical Specific Energy

SDS   Small Drilling Simulator

LDS   Large Drilling Simulator

Symbols/Abbreviations related to Bond Graphs

R   Resistor element

C   Capacitive element

I   Inertial element

SF   Source of Flow

SE   Source of Effort

MSF   Modulated Source of Flow

MSE   Modulated Source of Effort

TF   Transformer element

GY   Gyrator element

Chapter 1   Introduction

1.1. Background

Drilling process has been suffering minor to catastrophic failures resulting from downhole vibrations and preventing this unwanted phenomenon has been the primary goal of many experiments and field applications in order to maximize the drilling rate. Although the downhole vibrations can be controlled with the alteration of surface parameters like torque and weight on bit, often times, this leads to compromising the overall drilling performance. It is therefore crucial to understand the mechanism of drill string vibration so that we can harness these vibrations to enhance the drilling performance while mitigating its adverse effects. Many tools and downhole equipment have been developed with the goal of generating or harnessing the downhole vibrations and passive-Vibration Assisted Rotary Drilling (p-VARD) tool is one of them.

1.2. Research Context and Motivation

One of the main research streams at the Drilling Technology Laboratory of Memorial University of Newfoundland is concentrated in enhancing the ways to harness the vibrations in the drill string. P-VARD tool is the outcome of more than a decade long research work, which is concentrated in drill string vibration. There have been several experiments and field trials that have shown significant improvements in drilling rate by the use of p-VARD tool. However, the dynamics of the tool itself, in particular regarding natural frequency, resonance, vibration attenuation, damping and fatigue analysis have not been fully investigated to date. This work is tackled with the bond graph analysis of the p-VARD tool in this thesis with the motivation that it would be a key element

of p-VARD tool configuration for any drilling scenario. Bond graph is a powerful tool which can be used to simulate a multibody system. Results from the bond graph analysis of the p-VARD tool show that the natural frequency of the drill string is lowered to a workable range when using the p-VARD tool. Also, various operating parameters like WOB and RPM and tool parameters like spring configuration and damping ratio are identified as the variables that can control the resonance of the tool. The results from the dynamic analysis of the p-VARD tool can be used to design the optimal experimental setups.

To date, most p-VARD laboratory characterization has utilized the Small Drilling Simulator (SDS). Currently, the Drilling Technology Laboratory at the Memorial University of Newfoundland is migrating drilling researches to the much sophisticated, state of the art Large Drilling Simulator (LDS), which is fully instrumented, can be operated automatically or manually and has order of magnitude increased in available WOB, rotary speeds and drilling torque. Performing the p-VARD experiments in the LDS will enable us to understand the characteristic of the tool in more depth and this is the research motivation behind the design analysis of the LDS p-VARD tool. The p-VARD experiments in the LDS will be more versatile and include a wide range of operating parameters and tool parameters.

One of the factors that the p-VARD dynamic modeling does not consider is the spring friction. This is a crucial factor in case of p-VARD tool because the high frequency of spring compression will escalate the amount of frictional dissipation in the springs and result in the spring curves that are different from the ones generated by the simulation. Moreover, excluding the spring friction in the p-VARD dynamic modeling prevents us from analyzing the effect of spring lubrication on the overall performance of the tool. The characterization of the effect of spring friction/lubrication is

2

the motivation behind the development of a method to express frictional losses in Belleville springs in terms of the parameters related to spring and its stacking configuration. The new frictional model will enable us to analyze the dynamic impacts of having varying levels of friction and tool lubrication. The bond graph analysis of p-VARD tool with the modified spring model will generate more accurate results and take us a step closer towards fully characterizing the p-VARD tool.

1.3. Thesis outline

This thesis has seven chapter in total and this chapter provides an overview of the contents of all the chapter of the thesis. Additionally, the research motivation and goals are briefly highlighted in this chapter but are explained in more detail in each chapter. The contents of this thesis are based upon two manuscripts, which have been accepted for publication in the Canadian Society of Mechanical Engineers (CSME) 2020 Online Publication under the title of ***"Progress in Canadian Mechanical Engineering 2020"*** and American Society of Mechanical Engineers (ASME) 39th International Conference on ***Ocean, Offshore and Artic Engineering 2020*** (OAME). In addition to these, the works related to design analysis of p-VARD tool for the Large Drilling Simulator of Drilling Technology Laboratory is also included in this thesis.

Chapter 2 is the **Literature Review** that covers all the background materials related to drill string vibration, bond graphs, Belleville springs and p-VARD tool and is divided into 4 sub-sections accordingly. The sub-section related to drill string vibration provides a review of papers related to drill string modeling and the approaches followed by the researchers. Similarly, bond graph sub-section explains all the basics information related to the elements of the bond graph and the sub-section related to Belleville springs includes the explanation of spring dimensions and a review of

3

load-deflection curves and various fields of application. Finally, p-VARD tool sub-sections provide a review of papers related p-VARD experiments and simulation.

Chapter 3 is the **Bond Graph Modelling**, which explains the bond graph generation process. An example of a mechanical system is used to illustrate the steps involved in making of a bond graph. This work is the foundation to understand the bond graph analysis presented in Chapter 4.

Chapter 4 is the **Bond graph analysis of the p-VARD tool**. The bond graphs of rigid and compliant drilling systems are constructed in 20-sim based on the foundation setup by Chapter 2 and Chapter 3. The models are generated for the SDS drill rig with and without the p-VARD tool. 20-sim's parameter sweep is used to study the effect of different parameters on the system response. Results from this analysis help us understand dynamic behaviour of the p-VARD tool.

In **Chapter 5**, **Frictional losses in Belleville springs is calculated by Linear Interpolation method**. The effect of change in springs parameters like diameter ratio and free-height to thickness ratio is studied along with the identification of different kinds of Belleville springs. The work is further extended to analyze the Belleville springs used in the LDS p-VARD tool.

Chapter 6 is the **Design and Analysis of LDS p-VARD tool**. The tasks related to the finite element analysis of the p-VARD tool along with the specifications of p-VARD Belleville springs is included in this chapter. Moreover, the components of the LDS p-VARD tool are explained in detail with pictorial illustrations of the CAD model.

Lastly, **Chapter 7** is the **Conclusion and Recommendations**. The main findings and summary of each work is reiterated here along with future scope of work.

Chapter 2   Literature Review

This chapter is divided into four sub-categories, each providing a detail review of works related to Drill string vibration, Bond graphs, Belleville springs and p-VARD tool. In the first section, different modeling approaches for drill string vibration are explained, followed by the introduction to Bond Graphs and review of relevant works in the second section. An in-depth review of the works in the field of Belleville springs put together in the third section and review of field and experimental works related to p-VARD is presented in the last section.

2.1. Vibration in Drill String

The study and mitigation of drill string vibration has been the topic of interest for many drillers in oil fields and mining industries for a long time. A drill string exhibits a complex dynamic behaviour as it transmits the rotary motion from the surface to the drill bit, which was first discovered when using Measurement While Drilling (MWD) tools in 1990s [1]. A drill string also functions to transmit the axial force called Weight on Bit (WOB) and the drilling fluid to the drill bit. A schematic of a typical drilling rig shown in Figure 1 shows the major components like draw works, hoisting system, drill-mud circulation system, derrick, and the rotary table.

There are three main types of drill string vibration, viz; axial, torsional and lateral vibrations and these vibrations may result in the phenomenon like bit-bounce, stick-slip or whirling [2] as shown in Figure 2. These are also identified as the main cause of high production cost and low penetration rates [3].
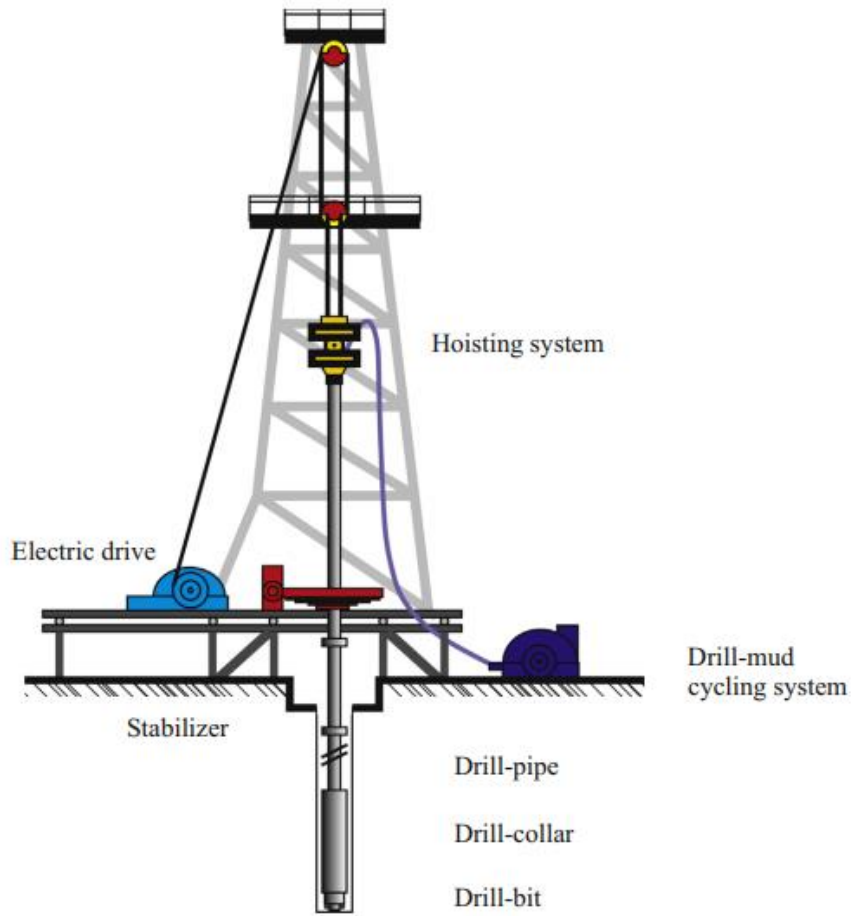
Figure 1: Schematic of a drilling system [1]

2.1.1. Axial Vibration

The main reasons of axial vibration are known to be the WOB variation, variation in fluid pressure and the bit-rock interaction forces [4]. The drill string moves along its longitudinal direction, which causes the BHA to bounce on the rock formation. This kind of vibration is mostly known to occur in roller cone bits when drilling in hard formations or when the formation changes. Furthermore, they can be identified by the high levels of fluctuations in WOB or large vibration measured

6

through surface measurement devices or MWD tools. At shallow depths, this kind of vibration can be observed at surface in the form of hook load variation and bouncing of the Kelly or the TDS [5]. In a paper by Spanos et. al. 1995 [6], an analytical model of a drill string is built using a mass-spring-damper element [Figure 3]. The model of the drill pipes and drill collars is discretized into finite number of elements and a set of equations is built using the dynamic matrix approach to obtain the analytical solution as:

$$M\ddot{X} + C\omega\dot{X} + KX = P$$

where M is global mass matrix, X is generalized displacement vector, C is golbal damping matrix, ω is frequency of vibration, K is global stiffness matrix, and P is generalized load vector
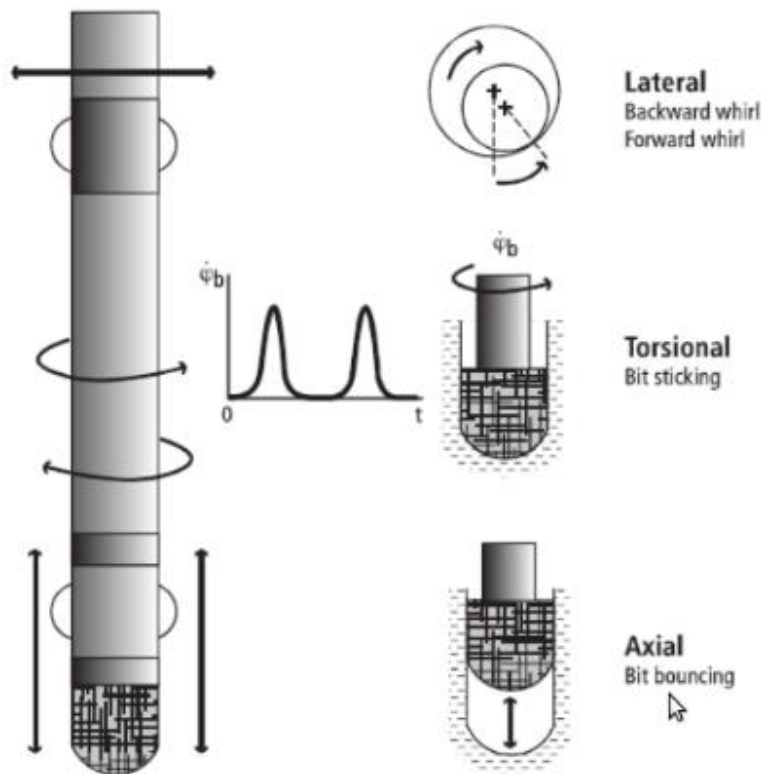
Figure 2: Showing types of vibration in a drill string [2]

7
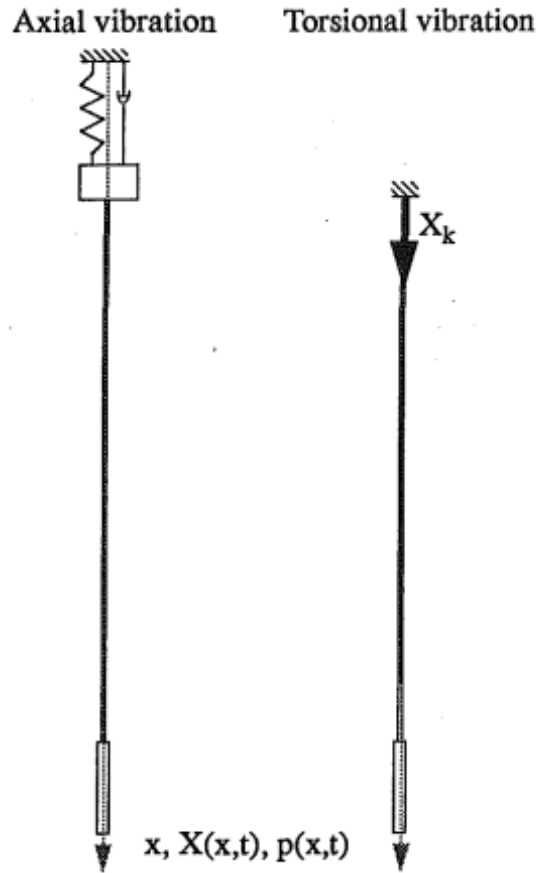
Figure 3: Mass-spring-damper model of drill string for axial torsional vibration [6]

2.1.2. Torsional Vibration

A severe form of torsional vibration leads to stick-slip phenomenon. In one of the recent works related to the study of stick-slip vibration, Yang et. al 2019 [3] have used the generalized lumped-parameter model showing the existence of multi-stability with regards to stick-slip, constant rotation and bit sticking. This work also highlights that the main cause of the stick-slip vibration as the frictional force acting at the bit-rock interface. Schematics of the drill string used by the authors to model the stick-slip vibration is shown in Figure 4, where $\dot{\phi}$ is the angular velocity, J_p is

the moment of inertia of the plates, k_p is the torsional stiffness, c_p is the angular damping, T_b is

the torque due to friction and u is the top drive torque. One of the advantages of using this method

to model a drill string that any addition of a drill pipe can be easily modeled by adding a rotating

disc to account for the change in length. The authors have concluded that there exists a reason

called the attractive region, which plays an important role in knowing if multiple state of bit

sticking, stick-slip and constant rotation is occurring. The chances of multi-stability increases as

the drilling depth increases. Stick-slip vibration is most common with PDC drill bits but is also

dependent upon formation properties. Combination of drilling parameters like low rotary speed

and high WOB is more likely to cause this kind of vibration [3].
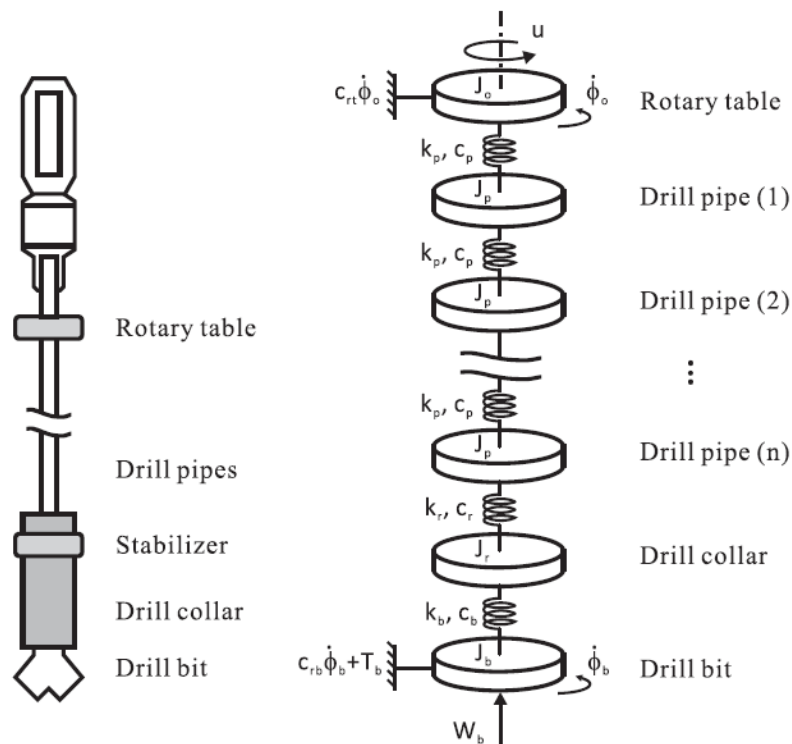
Figure 4: Schematics of a drill string using generalized lumped-parameter model [3]

The analysis of drill string vibration involves careful modeling of its material properties and the understanding of the interaction with the external factors. These studies can be done experimentally in a laboratory or field or through simulation techniques. Stick-slip vibration is most common with PDC drill bits but is also dependent upon formation properties. Combination of drilling parameters like low rotary speed and high WOB is more likely to cause this kind of vibration [3]. This section summarizes review of the works, which have been done to understand the vibration in a drill string.

2.1.3.   Lateral Vibration

The cause of lateral vibration is hard to pinpoint but it is mostly linked to the operations at certain critical rotary speeds [7]. Lateral vibrations are known to be the most damaging as it creates uneven wear on the drill string components. During lateral vibration, the BHA components collides with the borehole wall at high velocity increasing their chances of failure due to shock loads. In a paper by Kriesels et. al. 1999 [7], the authors describe how vibration analysis software like Drill String Dynamics (DSD) is able to calculate the critical velocity range for different configuration of the BHA using harmonic analysis. A driller can control the lateral vibration by adjusting the position of stabilizers which optimizes the buckling resistivity of the drill string [7]. Lateral vibration can occur in the form of Bit Whirl or BHA Whirl and in forward or backward direction [8]. Figure 5 shows the whirling motion in forward and backward direction.
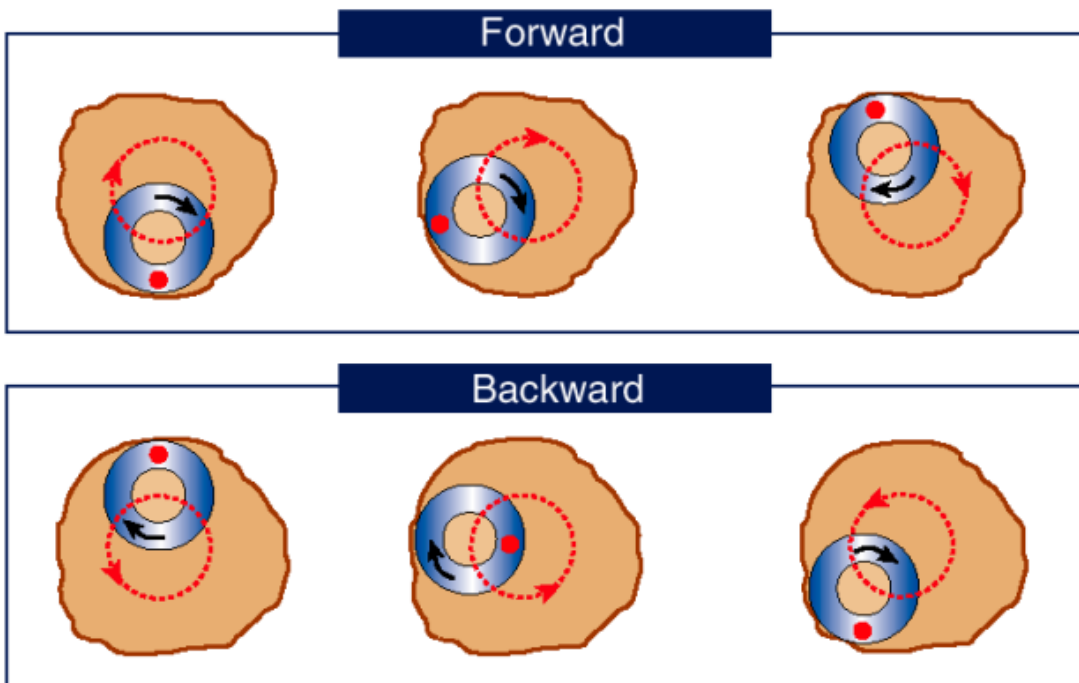
Figure 5: Showing forward and backward whirling motion [8]

2.2. Bond Graph

Bond graph is an interdisciplinary tool introduced by Henry M. Paynter in 1950s [9]. When bond graphs were introduced at first, the rules for power direction and causality were not well defined, as they are now. In 1960s bond graph notation was further improved by D. Karnopp [10] with the introduction of half arrows to identify positive direction of power flow. Bond graphs help in developing a dynamic model of a system using the universal currency of physical systems, power. This is a kind of graphical modeling language, which has different elements from mechanical, electrical, thermos-fluid or magnetic fields represented with generalized energy storage, dissipation or transfer elements. These elements are connected with power bonds, where signals are transmitted through them with 'effort' and 'flow' as its signals carriers. Table 1 shows the different terminologies used to represent these signal carriers in different fields.

Table 1: Effort and Flow of different domains

Energy Domain	Effort	Flow
Mechanical	Force (F)	Velocity (v)
	Torque (τ)	Angular velocity (ω)
Electrical	Voltage (V)	Current (i)
Hydraulic	Pressure (P)	Volume flow rate (dQ/dt)
Thermal	Temperature (T)	Entropy change rate (ds/dt)
	Pressure (P)	Volume change rate (dV/dt)
Chemical	Chemical potential (μ)	Mole flow rate (dN/dt)
	Enthalpy (h)	Mass flow rate (dm/dt)
Magnetic	Magneto motive force (e_m)	Magnetic flux (φ)

A generalized quantity is used to represent different elements in all energy domains. These quantities may be effort (e), flow (f), momentum (p) or displacement (q). Power is expressed as the product of effort and flow variable, i.e. $P = e(t) f(t)$. Similarly, momentum is expressed as the integral of effort and displacement is expressed as the integral of flow respectively.

Bond graph uses a list of generalized elements to develop a dynamic model of a system. The nature of these elements are same irrespective of the energy domain of interest. For example a *capacitor element* in translational mechanical domain is a *spring* where as it is an *open tank* in fluid domain. There are eight basic elements which are used to construct bond graph of any dynamic system viz; *Capacitive, Dissipative, Inductive, Sources, Transformer, Gyrator, Kirchhoff's loop and Kirchhoff's node* [11]. These elements may have single or multiple ports, where *power bonds* are connected to link the element to the rest of the system. Each *power bond* has a *half arrow* to determine the positive power flow direction and a *casual stroke* to indicate the input variable to the element's constitutive law equation. The location of casual stroke is independent of the half arrows and is related to the input-output form of the equation. The rule that governs the flow of effort and flow in a power bond is that the end of the bond that does not have the casual stroke is the end where flow is the input signal and effort is the output signal. An example of power bond, half arrow and casual stroke is given in Figure 6.
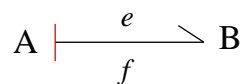
Figure 6: Illustration of power bond, half arrow and casual stroke

In the above bond graph, the half arrow indicates that positive power flow direction is from element A to B. Similarly, location of the casual stroke suggests that effort is an input to element A while flow is an input to element B. All elements have a preferred location of the casual stroke; if or when the casual strokes are inverted, it is called *differential causality* or else it is called *integral causality*. Next, the bond graph elements are categorized into active elements, passive elements, converters and junctions.

2.2.1. Active Elements

Active elements supply the energy when connected to the rest of the system. An active element may be a source of effort (SE) or source of flow (SF). A source of effort of source of flow can provide only one component of the power variable and the rest of the system determines the other component. For example, a flow source can only provide a specific level of flow, the value of effort depend on the energy demand of the rest of the system.

i.   *Source of Effort (SE)*

An ideal source of effort supplies a constant effort (e) to the system, independent of the energy drain from the source. The SE element defines the energy flow of the power bond where as the rest of the system determined the value of the flow parameter. An example of source of effort in mechanical system can be Force or Torque. SE is a single port element with effort-out preferred causality as shown in Figure 7.

$$SE \xrightarrow[\quad f \quad]{\quad e \quad}| \quad \text{rest of the system}$$

Figure 7: Source of effort with preferred causality

ii.   Source of Flow (SF)

Source of Flow imposes a flow on the system; the effort is determined by the response of the system. Sources of flow may be linear velocity, angular velocity, electrical current or volumetric flow rate depending upon the energy domain of interest. Since a flow must be imposed on the system, the preferred location of the casual stroke is the port at the element as shown in Figure 8.

$$\text{SF} \quad\xrightarrow[f]{e}\quad \text{rest of the system}$$
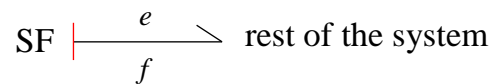
Figure 8: Source of flow with preferred causality

2.2.2.   Passive Elements

Passive elements receive energy from the system. A passive element is a single port element and it may be a capacitive, dissipative or inductive. Depending upon the nature of the element, a passive element may either dissipate or store the energy.

i.   Capacitive element (C)

These elements are also known as the compliance elements as they store potential energy. The main characteristics of these elements is that effort is directly proportional to the displacement and is related as:

$$e = \frac{1}{C}\,q$$

Where e is effort, q is displacement and C is compliance

15

Capacitive elements have flow in preferred causality as shown in Figure 9. Examples of a capacitive elements are spring (mechanical), capacitor (electrical) or open-tank (hydraulic).

$$C \quad \angle \overline{\frac{e}{f}} \rightarrow \text{rest of the system}$$
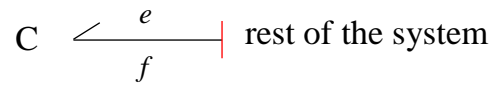
Figure 9: Preferred causality of a capacitive element

ii. *Resistive element (R)*

A resistive element dissipates the energy to the environment and relates its effort and flow as $e = \emptyset(f)$. Most of the physical examples of resistive elements can be represented by a linear function of $\emptyset$. However, bond graph makes it handy to solve the dynamic systems with non-linear relationship between the effort and flow variables. This element does not have a preferred causality. Common examples of R element are damper (mechanical), resistor (electrical) and fluid friction (hydraulic).

$$R \quad \angle \overline{\frac{e}{f}} \rightarrow \text{rest of the system}$$

$$R \quad \overline{\frac{e}{f}} \leftarrow \text{rest of the system}$$
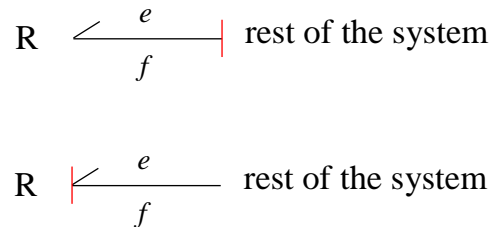
Figure 10: Preferred causality of a resistive element

iii. *Inductive element (I)*

Inductive or inertial elements store energy in the form of kinetic energy and exhibits a relationship between flow and momentum variables. Although this relation is non-linear in most cases, a general linear assumption can be made for most practical cases to derive the relation between flow

16

and momentum variable as $f = (1/I) * p$, where I is the inductance. Another equation that relates the effort (e) to momentum (p) in inertial elements is $e = \dot{p}$. Some of the common examples of inductive elements of different domains are mass (mechanical), inductor (electrical) and fluid inertia (hydraulic). The preferred causality of an inductive element is flow-out, effort-in as shown in Figure 11.

$$I \quad \xleftarrow{\quad e \quad}_{f} \quad \text{rest of the system}$$
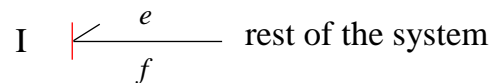
Figure 11: Preferred causality of an Inertial Element

2.2.3. Two Port Elements

These are the energy converting elements, where energy flows in from one port and is transferred to the output port. Ideally, these elements follow the laws of conservation of energy with input energy equal to the output energy; if e_1 and f_1 are the effort and flow at input port and e_2 and f_2 are the effort and flow at the output port, then $e_1 f_1 = e_2 f_2$. *Transformer* and *Gyrator*, which are two types of the two port elements, the main difference between them being the preferred causality.

i.   Transformer (TF)

These elements relate input effort to output effort and input flow to output flow. The preferred causality of a transformer element is effort-in effort-out or flow-in flow-out. In an effort-in effort-out causality, output effort is directly proportional to the input effort and in a flow-in flow-out causality, output flow is directly proportional to input flow. The proportionality constant in both cases is called the transformer module (k_t).

Figure 12 illustrates the preferred causality for a transformer element with their respective relationships.

$$e_2 = k_t e_1$$
$$f_1 = k_t f_2$$

$$e_1 = k_t e_2$$
$$f_2 = k_t f_1$$
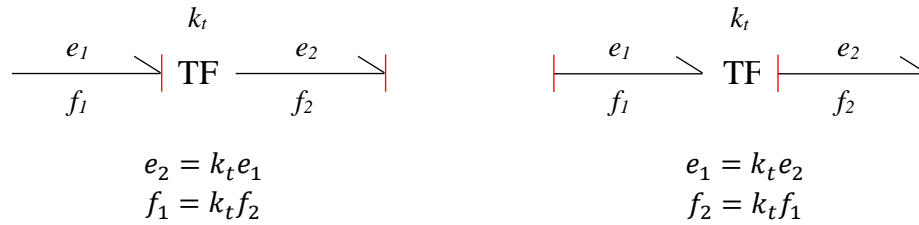
Figure 12: Showing preferred causalities of a Transformer element

Examples of transformer element are lever (mechanical), transformer (electrical) and venture (hydraulic). A transformer can also transform the energy from one domain to another. Examples of such multi-domain transformers are rack and pinion, hydraulic pistons, voice coil, etc.

ii.   Gyrator (GY)

This two port element relates input effort to output flow or input flow to output effort with a proportionality constant known as the gyrator ratio (k_g). A common example of a gyrator is a DC motor, in which the output torque is directly proportional to the input current and output speed is directly proportional to the input voltage. Figure 13 shows the bond graph of gyrator element with its preferred causality and corresponding relationships.

$$f_1 = k_g e_2$$
$$f_2 = k_t e_1$$

$$e_1 = k_g f_2$$
$$e_2 = k_t f_1$$
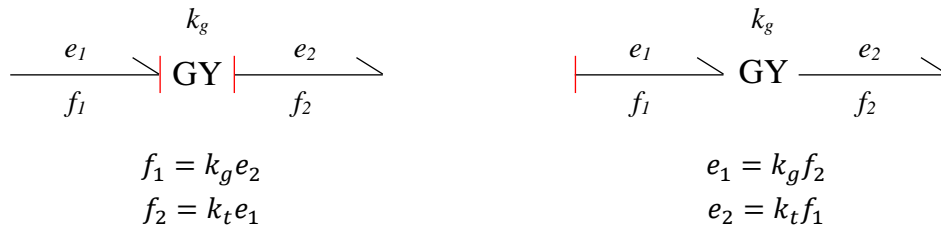
Figure 13: Showing preferred causalities of a Gyrator element

2.2.4. Junctions

There are two kind of junctions in bond graph, viz; 0-junction and 1-junction. Both junctions follow the laws of conservation of energy, which neither dissipates nor stores the energy. A basic sign convention for these junctions is that, if an arrow points towards the junction then the flow is assumed positive and if it points away from the junction, it is assumed negative. A strong bond for a junction is such bond, which is enough to determine the causalities of all other bonds in that junction.

i.   0-Junction

This is a common effort junction, which has identical effort in every bond. By definition, since these bonds are energy conserving elements, sum of flows in all its bonds must be equal to 0. The strong bond of a 0-junction has an effort-in causality and the effort in all other bonds is identical to it. Examples of 0-junction are electrical node, pipe intersection or force across a deformed spring. Figure 14 is a 0-junciton showing its strong bond and preferred causalities.

$$e_1 = e_2 = e_3$$
$$f_1 = f_2 + f_3$$
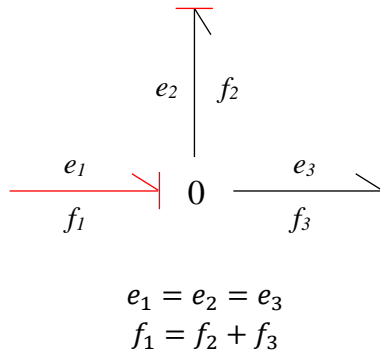
Figure 14: Showing bonds in a 0-junction

ii. *1-junction*

These are the common flow junctions with identical flow in every bond. A 1-junction acts like effort summing junction with where the strong bond is the one with flow-in causality. Examples of 1-junctions are parallel spring and damper, fluid flowing through a pipe, electrical circuit with no branches, etc. Figure 15 shows a 1-junction with a strong bond and its constituent equations.

$$f_1 = f_2 = f_3$$
$$e_1 = e_2 + e_3$$
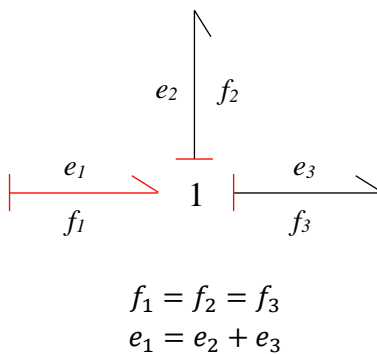
Figure 15: Showing bonds 1-junction

2.3. Belleville Springs

Belleville spring, patented and named after the inventor Julien Belleville in France in 1867 is one of the frequently used springs to support very large load with a small installation space. The use of Belleville springs has been proven to be beneficial in tackling the problems related to elastic interaction, creep, differential thermal expansion or in the isolation of seismic vibrations in bolted joints [12]. They have high spring rates, which is easily variable. This makes them suitable for using in different fields. One such use of Belleville springs in passive Vibration Assisted Rotary Drilling (p-VARD) tool is explained in much detail in Chapter 4 and Chapter 6.

Numerous works have been performed for better understanding the load-deflection nature of the Belleville springs. The first equation proposed by Almen-Lazlo [13] is the most cited and widely tested approach by several researchers and laboratories including General Motors Corporation. Researches which followed were mostly centered around the modification of the basis assumptions of Almen-Laszlo's theory. In the paper by J. Almen et. al. 1936 [13], the authors point out an important benefit of using a Belleville spring as a wide range of workable spring rates, which is unattainable with conventional coil springs.

Authors Zhiming et. al. 1990 [14] have used the theories of finite rotation and large deflection to generate a model for static response of a Belleville spring and diaphragm spring. The new mechanical model claims to capture the real spring scenario more accurately and is also backed by experimental results. Similarly, authors, Rosa et. al. 2001 [15] have based their discoveries on the ground that the radial stresses are linked to the tangential stresses by the equilibrium equation and designed a spring with variable thickness to obtain wide range of constant force over a range of

deflection. Similarly, with the development of experimental and simulation tools, new researches focused on the numerical analysis and FEA simulations of Belleville springs. In one of the works by Karakaya [16] the effect of material non-linearity was studied to enable the manufacturing of springs with composite material instead of conventional steel. Simulation techniques have made it possible to study the effect of tapered-ness in the spring design. Results from the work by Rosa et. al. [15] have shown possibility of manufacturing springs that are radially tapered thus increasing the linear region of the load-deflection curve, meaning that springs can be operated with higher range of constant loads. Apart from these, studies have also been done to study the effect of having slotted Belleville springs [17].

2.3.1. Types of Belleville springs

Depending upon the nature of the load-deflection curve, Belleville springs can be categorized into High Load, Standard, Force Limiting or Force Adjusting Belleville springs [18]. Different springs have different field of application. A very thick spring has almost linear form of load-deflection curve and as the spring gets thinner, the load-deflection curve becomes cubical, flat and even negative. These springs are explained in the following sections.

A. *High Load Belleville Spring*

These springs are very thick and are designed to withstand high load. The geometry of these springs is such that the OD to ID ratio and the free height to thickness ration are small. Greater thickness of these springs also result in higher fatigue life and make them suitable for static and dynamic loading. They are typically used in flange bolts to retain the load lost due to material creep.

B. *Standard Belleville Spring*

These type of Belleville springs are known for their high fatigue life. They are designed such that stress accumulation is very low making them suitable for dynamic loading. They are mostly used for vibration dampening, shock adsorption and for expansion compensation [18]. In terms of the load-deflection curve, these springs are linear at the beginning and become cubical before flattening.

C. Force Limiting Belleville Spring

These springs can provide a constant force after certain point while allowing some deflection. In a load-deflection curve, they start out linear and transition into flat after reaching certain amount of load. As the name of the spring suggests, they can exert a constant force for a range of spring deflection. This unique nature of force limiting Belleville spring makes it suitable for using in clutches, brakes and pressure relief valves. Another application of these springs is in the cableway grip.

D. Force Adjusting Belleville spring

These springs are designed such that the slope of the load-deflection curve becomes negative after certain amount of deflection. To obtain this unique nature, they are designed with high free height to thickness ratio, which result in high stress concentration and low fatigue life. They are commonly used in valves, to keep them sealed. When the valve is opened, the spring is compressed beyond its maximum load and will start to lose the force.

The four different kinds of springs along with the nature of their load-deflection curve are shown in Figure 16 and Figure 17 respectively.
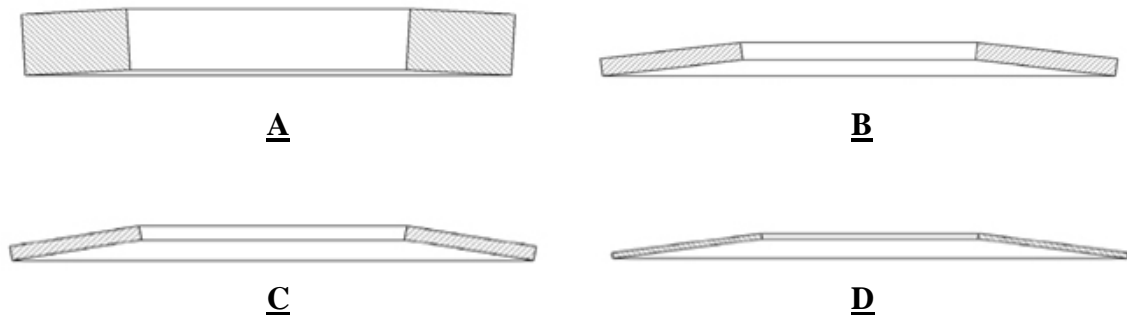
Figure 16: Showing A) High Load Belleville Spring, B) Standard Belleville Spring,
C) Force Limiting Belleville Spring and D) Force Adjusting Belleville Spring [18]
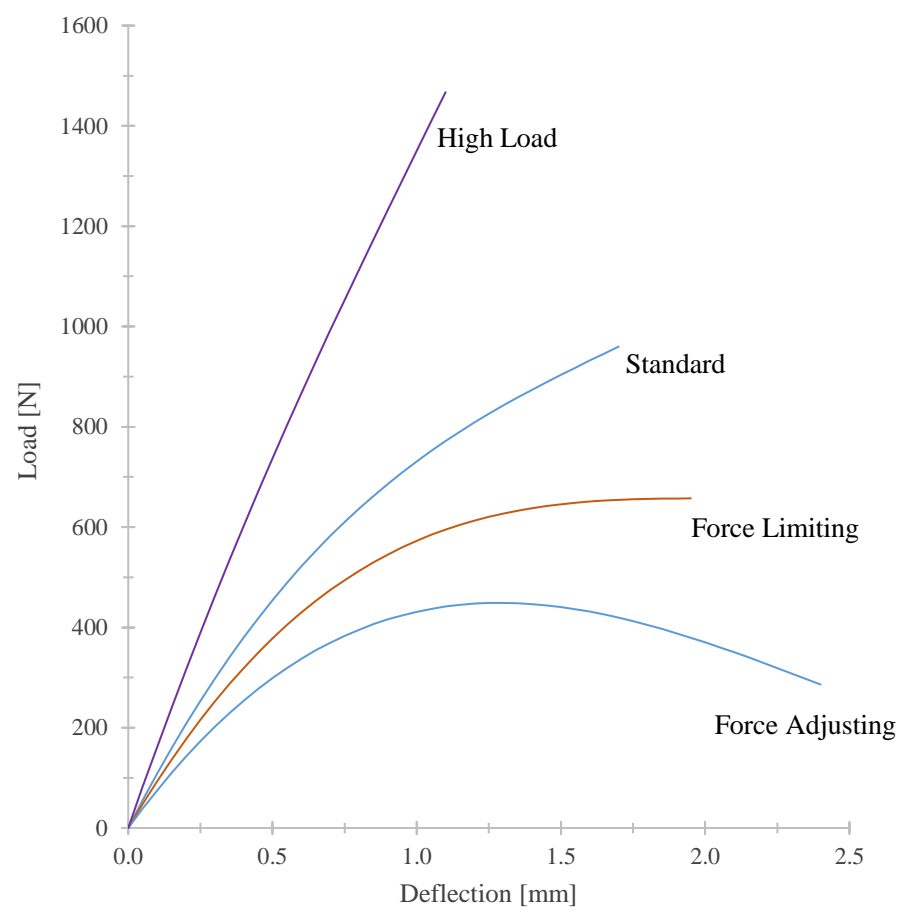
Figure 17: Load-deflection curves of different types of Belleville springs

The use of Belleville springs is very common and the field of application may be automotive, aircraft, piping or electrical, which is made up of a mechanical assembly. Use of Belleville springs in the busbars used in electrical switchgear or panel boards has enabled the operators to maintain required clamping pressures in the joints despite the material relaxation and vibration [12]. Similarly, Paredes et. al. 2010 [19] illustrates the use of Belleville springs in the ropeway braking system to keep it stationary when parked or during emergency stoppage. Apart from this, Coffman 2013 [20] explains his gun recoil assembly patent, which uses the combination of Belleville springs and the helical springs such that it not only preserves the recoil energy but also reduces the slide velocity resulting in minimal impact and damage to the firearm. The use of Belleville springs in automotive industry is even more common. Some of the units where Belleville springs are used are parking brakes, door hinges, drum brakes, clutches and motor foundations [21]. Similarly, the use of Belleville springs in manufacturing industry can be seen in the tool clamping components, commonly used in CNC devices. When the tool is inserted into the spindle, a stack of compressed springs locks the tool in position by pushing against the tool clamp, which is acted upon by the hydraulic system when it needs to be released [22]. The use of Belleville springs in automotive industry is even more common. Some of the units where Belleville springs are used are parking brakes, door hinges, drum brakes, clutches and motor foundations [21]. Similarly, the use of Belleville springs in manufacturing industry can be seen in the tool clamping components, commonly used in CNC devices. When the tool is inserted into the spindle, a stack of compressed springs locks the tool in position by pushing against the tool clamp, which is acted upon by the hydraulic system when it needs to be released [22].

Irrespective of the field of application or the mechanical assembly, the main use of Belleville springs comes from their ability to provide compliance to the system and/or store the energy. In upcoming sections, an introduction to load-deflection characteristics and frictional losses in Belleville springs is provided.

2.3.2. Load-Deflection Curve of Belleville Spring

To understand the different dimensions used to interpret a Belleville spring, one may refer to Figure 18. In the figure, H is the total height and h is the free height of the spring. When the spring is fully compressed, the total spring deflection is equal to the free height (h) of the spring, which is approximately equal to the difference between the total height (H) and the spring thickness (t). Very often, dimensionless variables such as diameter ratio (γ) and free height to thickness ratio (h/t) are used characterize the springs.
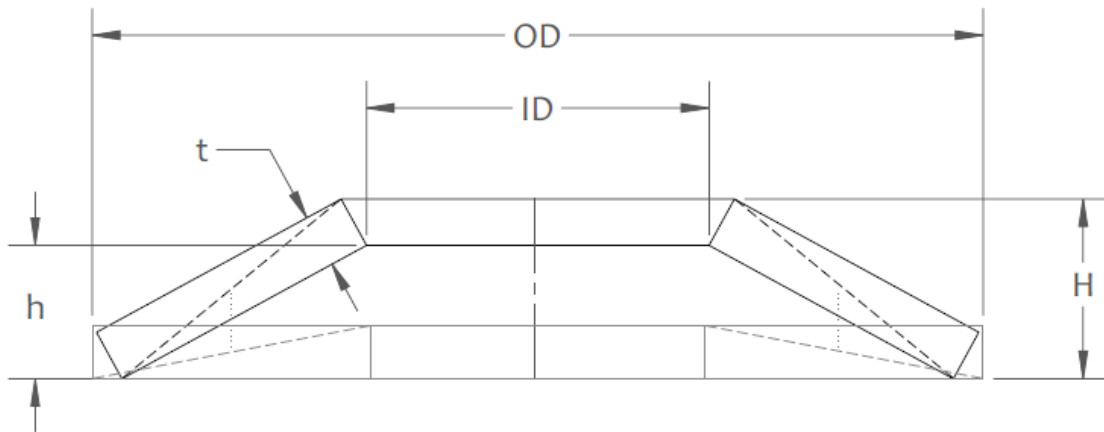
Figure 18: Showing different dimensions of a Belleville spring

The load-deflection curve proposed by Almen-Laszlo was dependent on three major assumptions:

    i.   Small angular deflection takes place at the spring cross-section

    ii.   Spring deflection takes place by mere rotation about a neutral point

    iii.   Loads are concentrically distributed, and radial stresses are negligible

Based on these assumptions, the relation proposed by Almen-Lazlo [13] for the load-deflection curve of a Belleville spring is:

$$P = \frac{E\delta}{(1 - \vartheta^2)\, r_2{}^2}\left[(h - \delta)\left(h - \frac{\delta}{2}\right)\frac{t}{M} + \frac{t^3}{N}\right] \qquad\text{.................................... (i)}$$

$$\text{where, } \frac{1}{M} = \left[\frac{\gamma + 1}{\gamma - 1} - \frac{2}{\ln\gamma}\right]\pi\left(\frac{\gamma}{\gamma - 1}\right)^2 \qquad\text{.................................... (ii)}$$

$$\frac{1}{N} = \frac{\pi}{6}\ln\gamma\left(\frac{\gamma}{\gamma - 1}\right)^2, \qquad\text{.................................... (iii)}$$

$$\gamma = \frac{r_2}{r_1} \qquad\text{.................................... (iv)}$$

One of the major advantages of using Belleville springs is their easy stacking. The load-deflection characteristics of the spring can be easily varied by varying the spring stacking. For example, adding springs in parallel makes the spring stack stiffer where as adding springs in series makes the spring stack more compliant. One may achieve desired load-deflection curve by altering the number of springs in series (I) and/or the number of springs in parallel (J). The equations proposed by Almen-Lazlo was modified by Ozaki et. al. [23] to incorporate the effect of spring stacking in terms of I, J and effective deflection $(\bar{\delta})$ as:

$$P = JP_m \qquad\text{.................................... (v)}$$

$$\text{where, } P_m = \frac{E\bar{\delta}}{(1-\vartheta^2)\,r_2{}^2}\left[(h-\bar{\delta})\left(h-\frac{\bar{\delta}}{2}\right)\frac{t}{M} + \frac{t^3}{N}\right] \qquad \dots\dots\dots\dots\dots\dots\dots\dots\dots\dots\dots\dots \text{ (vi)}$$

$$\bar{\delta} = \frac{\delta}{I} \qquad \dots\dots\dots\dots\dots\dots\dots\dots\dots\dots\dots\dots \text{ (vii)}$$

Stacking of multiple Belleville springs results in the modification of equivalent spring constant (P/δ) or the total deflection (δ). When the springs are stacked in the same direction, it is called parallel stacking and it produces more stiffness while maintaining same deflection. On the other hand, in series stacking, springs are arranged in alternating direction, which increases the compliance and the deflection. Figure 19 gives an image of how Belleville springs are stacked in series or parallel
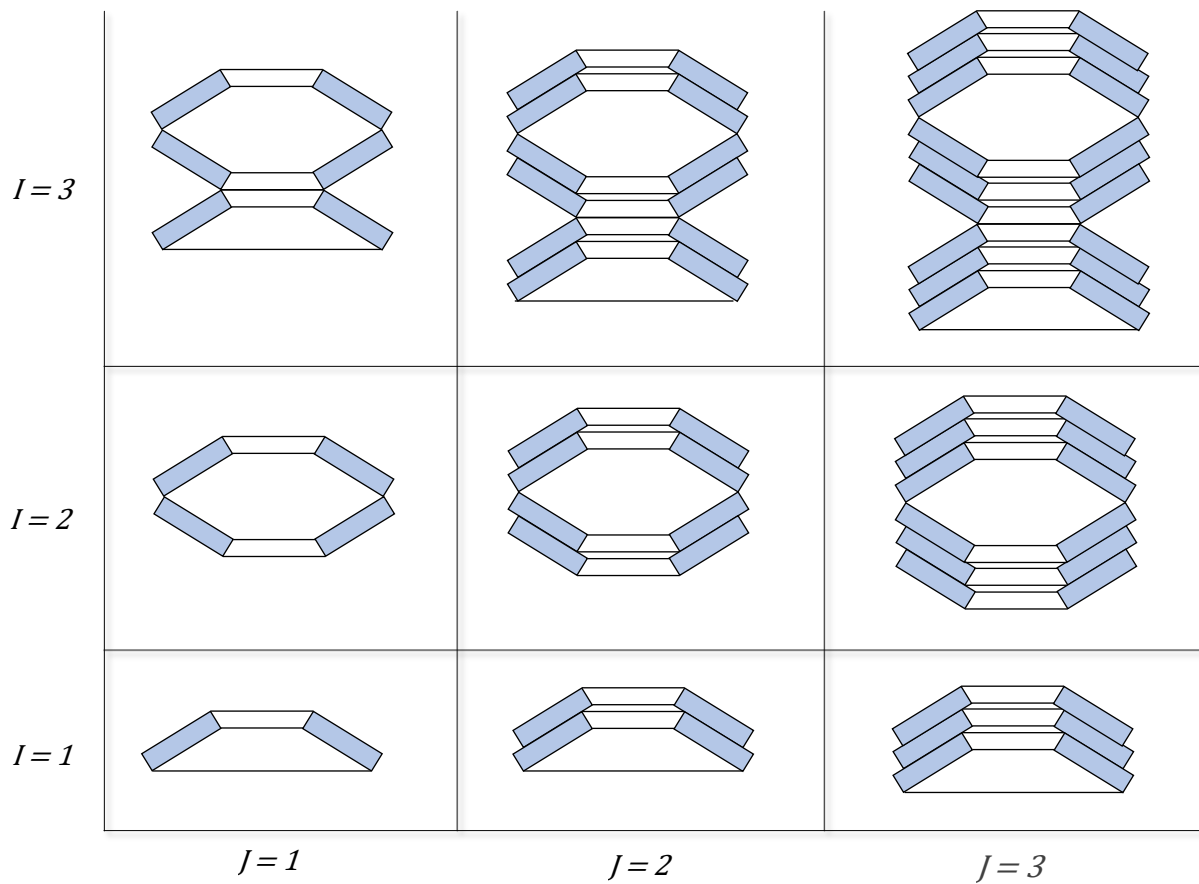
Figure 19: Series and parallel stacking of Belleville Springs

Although these configurations produce unique load-deflection characteristics, they follow the same principle of spring stacking, i.e. springs stacked in series result in compliant system where as springs stacked in parallel result in stiff system. In Figure 20, the effect of spring stacking in load-deflection curve is shown for different configurations.
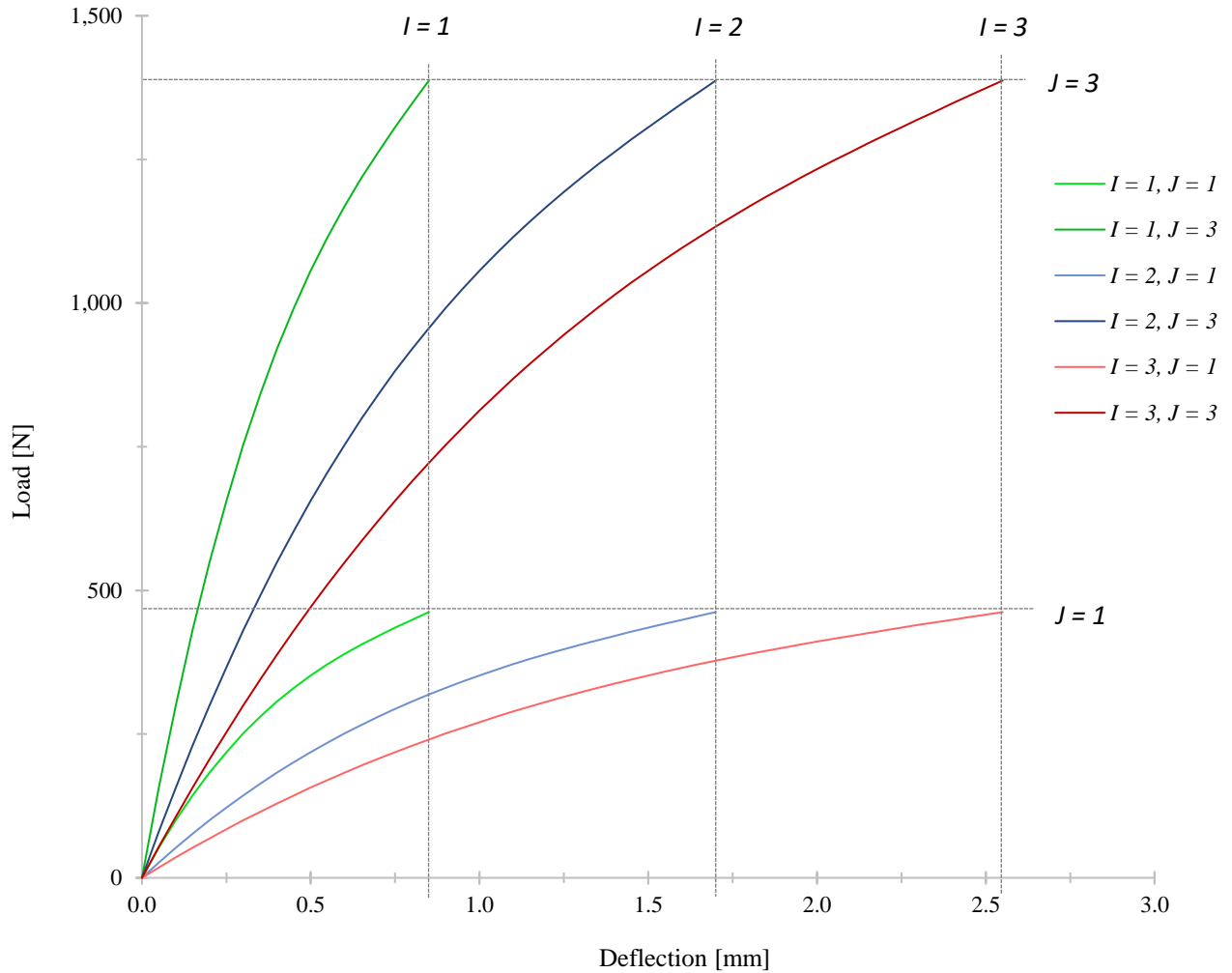
Figure 20: Load-deflection diagram for different configuration of Belleville springs
[Spring parameters (mm): H = 1.7, r_1 = 18.08, r_2 = 24.45, t = 0.85]

2.4. Passive Vibration Assisted Rotary Drilling (p-VARD) tool

The invention of p-VARD tool came as a result of extensive studies related to the effects of vibration in rotary drilling system. Figure 21 shows the p-VARD tool, which is designed for the Large Drilling Simulator of the Drilling Technology Laboratory, MUN. It highlights all the major components that make up the p-VARD tool and shows how the components are assembled.
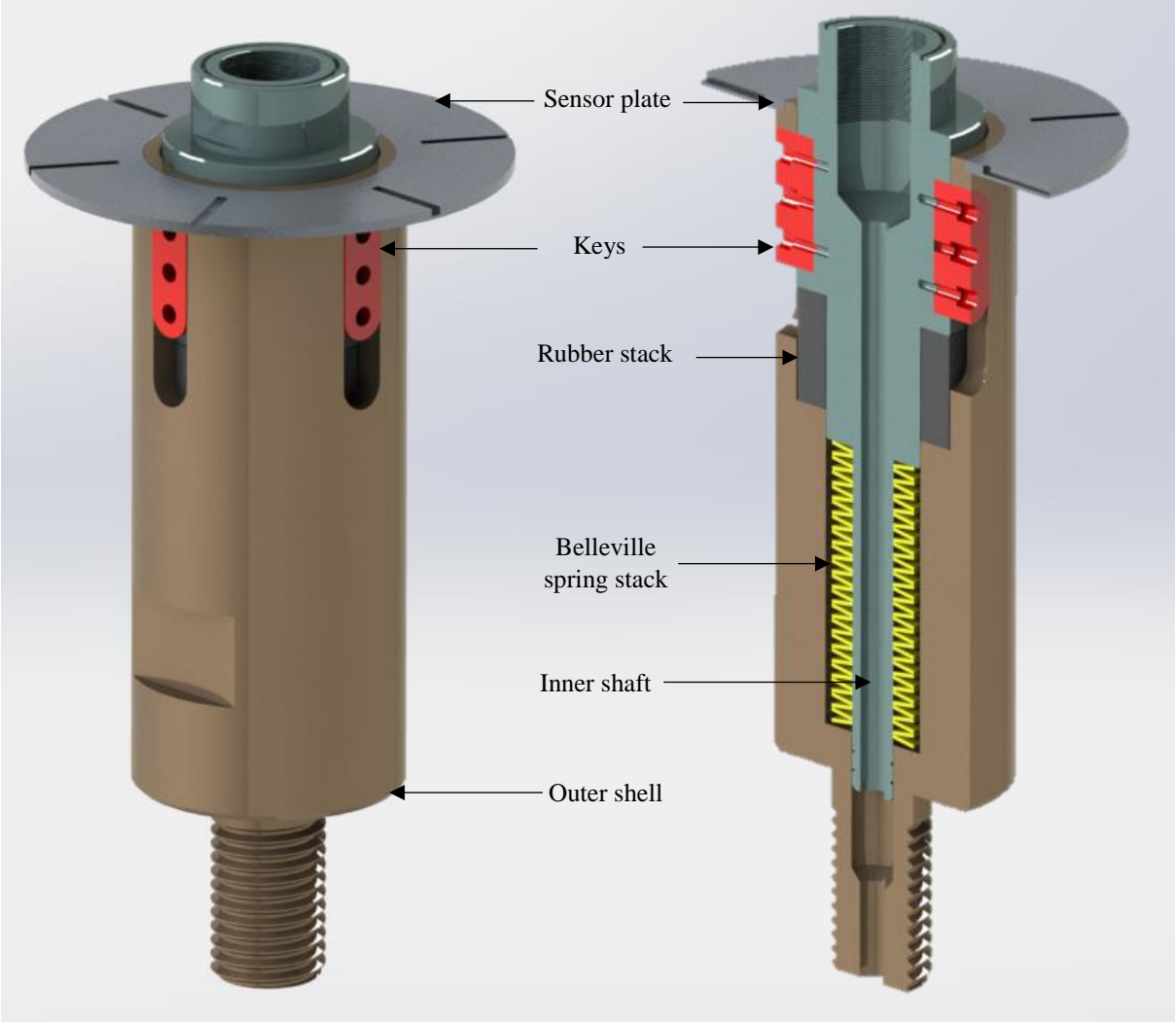
Figure 21: Showing major components of the LDS p-VARD tool

Although vibration in drill string is mostly known to cause bit bounce, stick-slip and whirl, there have been numerous researches that study the positive effect of vibrations in drill string (specially axial). In this part of the literature review, the works related to the p-VARD tool are summarized, highlighting their key findings and the nature of the study.

One of the early experimental evaluation of the p-VARD tool was done by Rana et. al. 2015 [24] and it reported an increase in ROP by more than 50% within the operational range of the tool. The experiments were performed using a 35 mm two-cutter PDC drill bit to drill on a fine-grained concrete samples with a UCS of approx. 50 MPa. Three p-VARD settings with high, medium and low compliance were tested against the conventional rigid drilling system. The authors have pointed out that p-VARD tool utilizes the bit-rock interaction force and generates useful axial vibrations that can enhance the drilling ROP. The experiments of this paper were performed in Small Drilling Simulator, which is explained in more detail in Section 4.2.

Similarly, Gillis and Butt 2018 [25] reported on the field trials using p-VARD tool as a part of the drill string BHA. A total of 1046 feet was drilled using an Ingersoll Rand drilling rig with a 6.5 inch PDC bit at a constant flow rate of 57.5 gpm [Figure 22]. The BHA also had a sensor sub to measure the downhole vibration data in addition to the full-scale p-VARD tool. The paper evaluates and compares the effects of p-VARD tool on the drilling mechanical specific energy (MSE) in the lab experiments and in the field trials. The authors have reported that use of p-VARD reduces the MSE and this is more significant in lab experiments because it is easier to control.
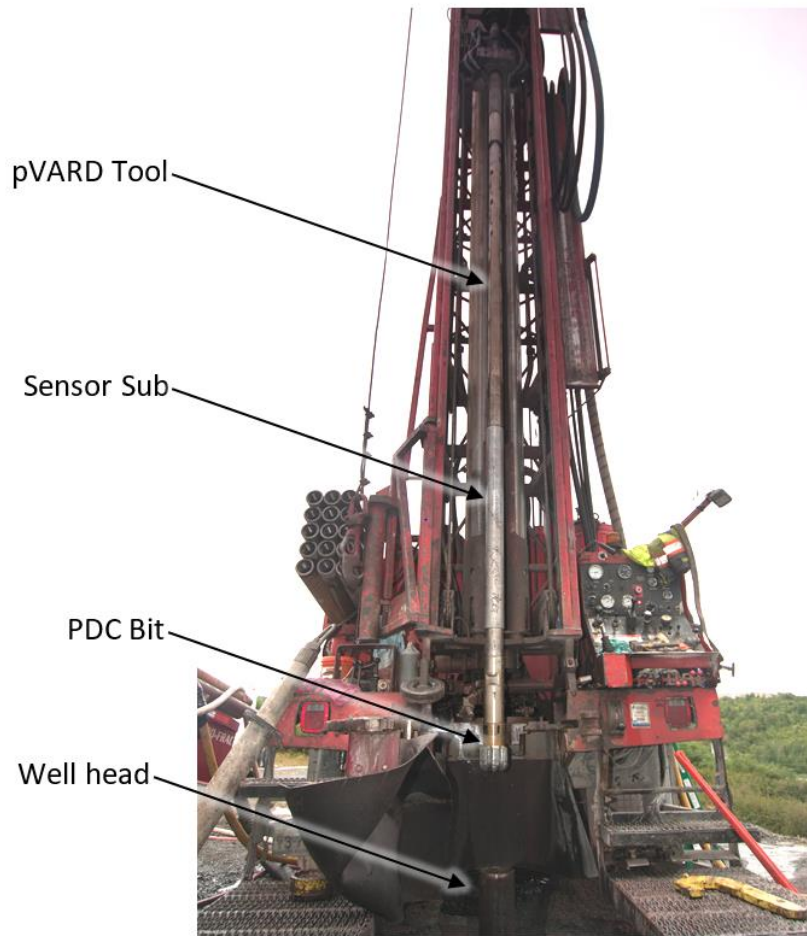
Figure 22: Ingersoll Rand drill rig, Field trials using p-VARD tool [25]

A different approach to evaluate the effects of p-VARD tool was presented by Alwaar et al. 2018 [26] using PFC-2D simulations. This work analyzes the laboratory experiments done by Rana et al. 2015 [24]. The input parameters for the study were the bottomhole pressure, WOB and the spring configuration while the output parameters were the ROP, DOC and the MSE. A simulation model was built in PFC-2D, where three balls represented the WOB and p-VARD spring stiffness and rubber damping [refer to Figure 23]. The authors have shown that the drill performance is

enhanced by the use of the p-VARD tool and is backed by the results from the Depth of Cut (DOC) and MSE analysis.
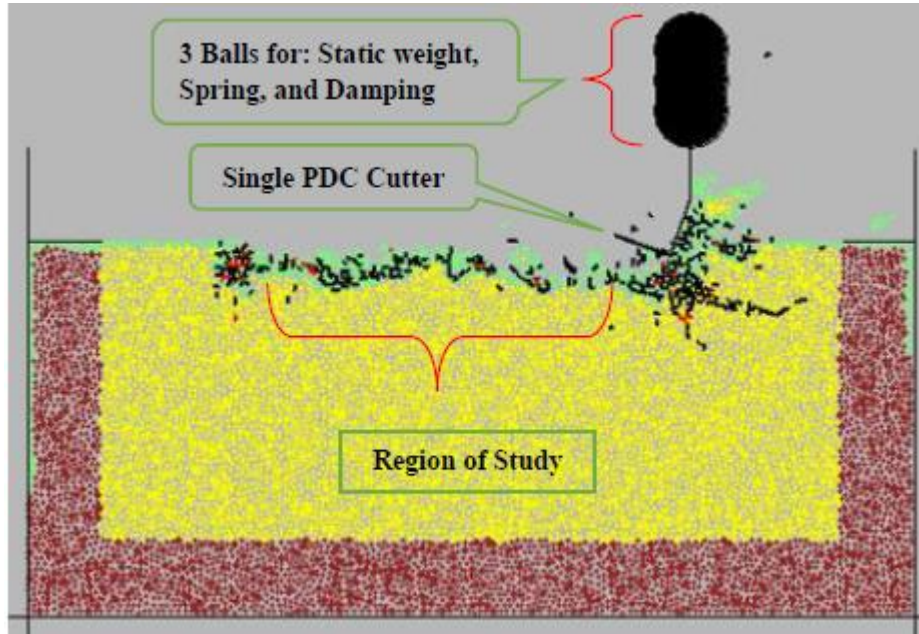
Figure 23: Simulation model of p-VARD tool in PFC-2D [26]

Another study of p-VARD tool was done by Shah et al. 2019 [27] to determine its effects in diamond core drilling. The experiments were performed using a 26 mm diamond core drill bit to drill into hard rock material with 145 MPa UCS in the Small Drill Simulator (explained in more detail in Section 4.2). The p-VARD tool was operated in three different settings, namely SinSoft, SinStiff and DouStiff [refer to Figure 24], which resulted in lower tool compliances. The authors have reported a maximum increase in ROP by 28% for the SinSoft spring configuration and have highlighted the potential of this tool in diamond core drilling.
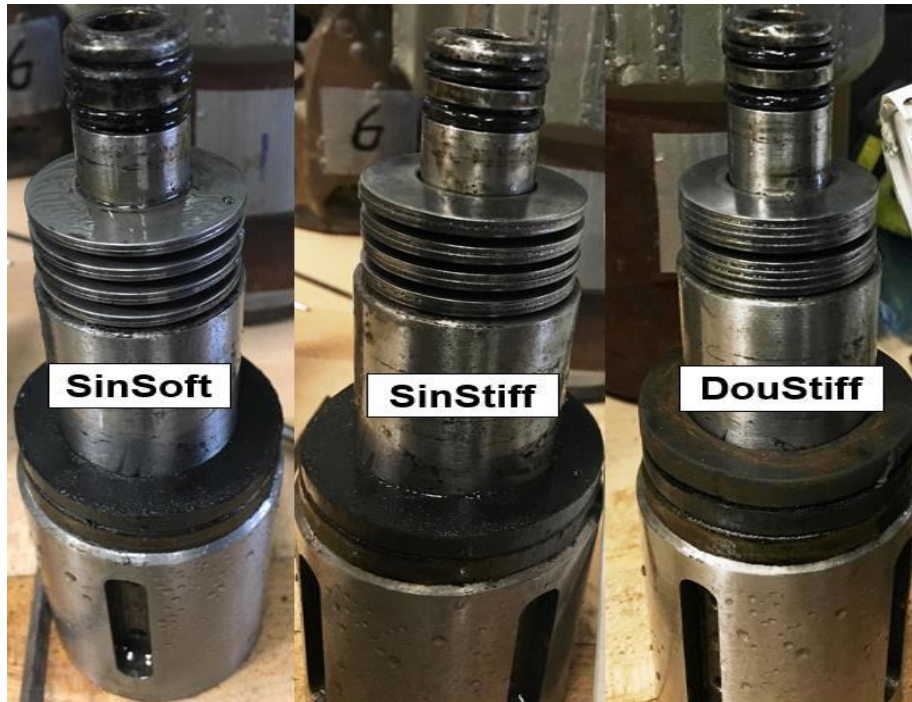
Figure 24: Belleville spring configurations in p-VARD tool [27]

In a series of drilling experiments by Molgaard et al. 2019 [28] a comparison of results between a rigid and compliant drill string was used to verify the positive effects of using the p-VARD tool. Experiments were done using a two-cutter PDC bit and diamond impregnated coring bit on shale rocks at a constant flow rate of 7 lit/min. Results from the experiments showed that p-VARD tool is more effective when drilling with a PDC bit than with a coring bit in shale formation. The authors have also reported in increase in Dynamic Downhole WOB when using a p-VARD tool.

Chapter 3   Bond Graph Modelling

3.1. Introduction

Until now, we have covered various aspects of Belleville springs, bond graph and drill string vibration in Chapter 2. In this chapter, we will generate bond graph of compliant drilling system of Chapter 4 - Figure 29. The compliant drilling system utilizes the p-VARD tool as a part of the drill string, which uses stacks of Belleville springs and rubbers to provide necessary compliance and damping. The main difference between the response of a Belleville spring and a coiled spring is that the Belleville spring stack exerts zero force when it is in tension, whereas the coiled spring exerts positive or negative force depending upon whether it is in compression or tension. Using bond graph to analyze this system is advantageous because the spring can be coded to replicate its conditional behaviour as.

If $\delta > 0$ then, $P = JP_m$

$$\text{where, } P_m = \frac{E\bar{\delta}}{(1 - \vartheta^2)\, r_2{}^2}\left[(h - \bar{\delta})\left(h - \frac{\bar{\delta}}{2}\right)\frac{t}{M} + \frac{t^3}{N}\right] \quad \& \quad \bar{\delta} = \frac{\delta}{I}$$

Else, $P = 0$

Before starting the construction of bond graph, first we lay out the steps to construct a bond graph of any generalized mechanical system.

3.2. Steps for generating a bond graph

The steps to generate a bond graph varies as per the energy domain. In this thesis, we discuss the generalized steps to generate a bond graph for translational/rotational energy domain. After the schematic of the physical system is drawn, we follow following steps to construct our bond graph [11]:

- Mark the preferred positive direction of distinct absolute velocities (linear or rotational) on the schematic of the physical system including the zero velocities at the fixed supports.

- Determine the positive direction of effort sources, flow sources and deflection of springs and dampers.

- For each identified absolute velocity, insert a 1-junction and label them accordingly as per the schematics.

- Attach elements to the 1-junction, as per the absolute velocity represented by the junction; the directionality of the power bonds connecting these elements should be such that positive power always flows into an element (I, R or C element).

- Eliminate the bonds with zero velocity to obtain simplified bond graph and assign appropriate element causality.

3.3. Constructing the bond graph

In this section, we will generate the bond graph of the compliant drilling system of Figure 29. The schematic diagram of the drilling system is constructed and all the velocity points are marked accordingly as shown in Figure 25. Using the procedure that has been put forth, the bond graph of the system is constructed as shown in Figure 26. The movement due to the bit-rock interaction is

represented by sinusoidal flow source, which is connected to the rest of the system through a stiff spring representing the formation stiffness. Due to the effect of gravity, each inertial element (I) also constitutes a source of effort representing its weight, which is bonded together with the I elements at its corresponding 1 junction. For more intensive analysis of the drilling system, the bond graphs in Chapter 4 have some additional elements built into them in order to perform the actions like differentiation, integration and to determine the maximum and minimum amplitudes of vibration. Also in Chapter 4, the elements of the p-VARD tool like rubbers have been simplified and represented with an equivalent damper and the parasitic damping have been used where necessary.
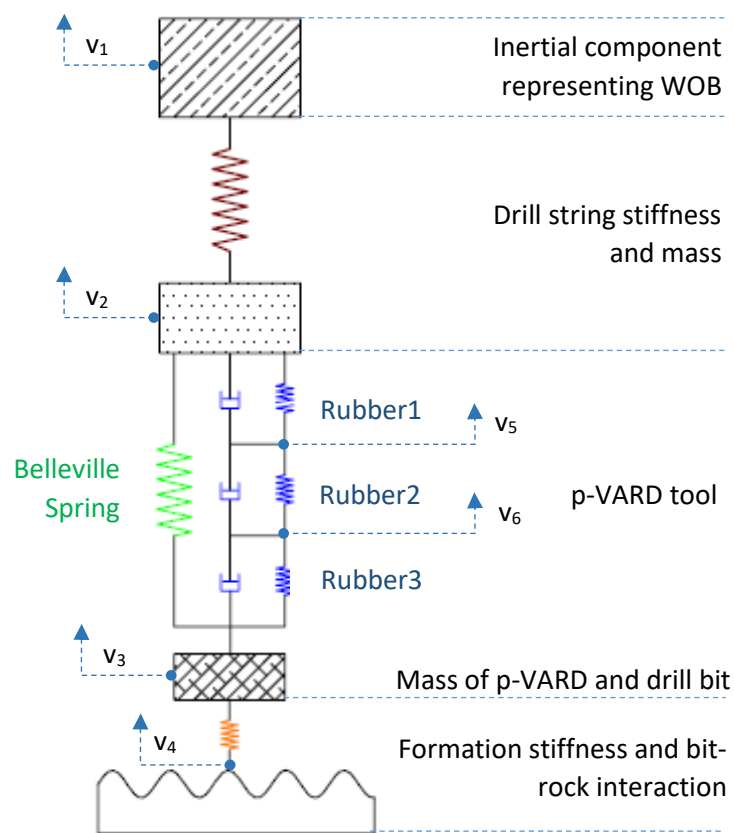
Figure 25: Schematic of compliant drilling system with p-VARD
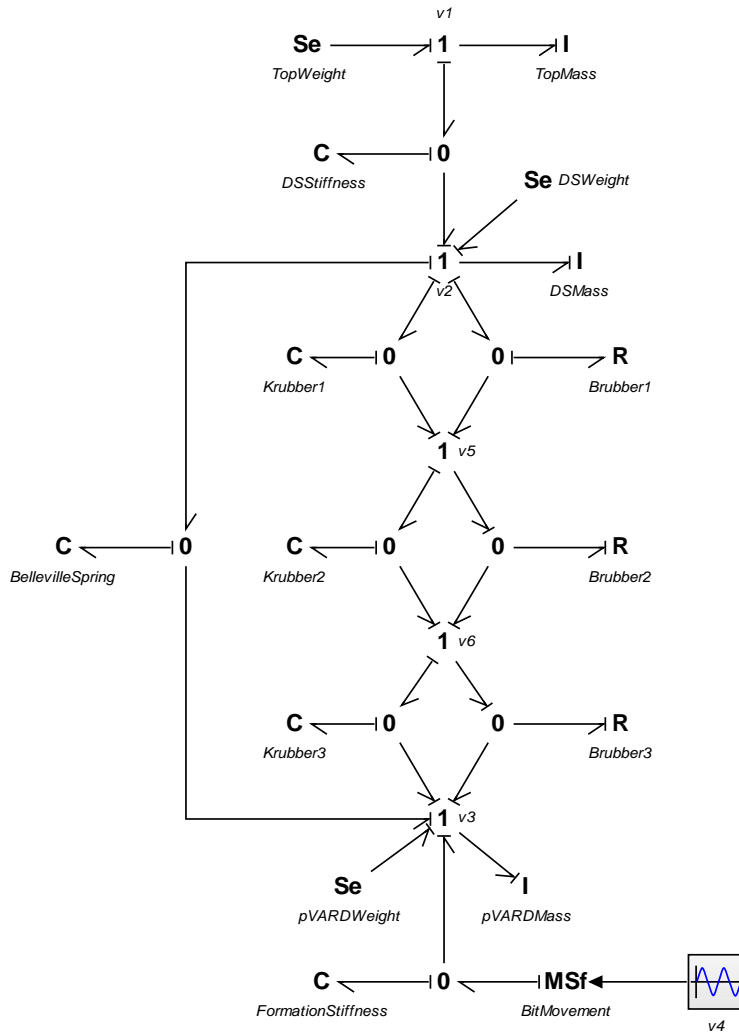
Figure 26: Preliminary bond graph of compliant drilling system

So far, the foundation work has been laid out to understand different steps involved in the bond graph generation and examples of two mechanical systems have been presented. In Chapter 4, we use the procedure described in this chapter to develop bond graphs of stiff and compliant drilling systems for the Small Drilling Simulator (SDS).

Chapter 4   Bond graph analysis of p-VARD tool

This chapter is based upon the paper titled *"Analysis of Passive Vibration Assisted Rotary Drilling Tool with the help of Bond Graphs"*, which has been published at the CSME 2020 Online Publication under the title of *"Progress in Canadian Mechanical Engineering 2020"*. This paper is co-authored with Jeronimo de Moura Junior, Dr. Geoff Rideout and Dr. Stephen Butt.

4.1. Introduction

The use of p-VARD to improve drilling performance has been experimented and well documented in many occasions. In addition to increasing the Dynamic Downhole Weight on Bit (DDWOB), the use of this tool has also reported in improving the drilling rate of penetration. The works until now are limited to experimental studies and lack the explanation as to how it actually works. Theoretically, adding a p-VARD tool increases the compliance of the drill string in an axial direction allowing the drill bit to oscillate axially. In this chapter, a mass-spring-damper bond graph model of p-VARD tool is built in 20-Sim. The spring is modelled with the help of Almen-Laszlo's load-deflection equation for Belleville springs and the damper is modelled as neoprene rubbers with moderate damping ratio. The bit-rock interaction is represented in the form of a source of flow providing sinusoidal displacement to the drill bit and the oscillating portion of the p-VARD tool. A parametric analysis of the drilling system consisting of a p-VARD tool shows that the resonating frequency of the system can be lowered to a workable range with the help of this tool thus allowing it to resonate and amplify the impact generated. Similarly, this modeling tool also enables us to study the parameters which may flatten the Belleville springs. A stack of flat springs is as stiff as the rigid drill string and this terminates the impact generated by the resonance. Results

39

show that spring and damper inside the p-VARD tool can be tuned to be operated at different Weight on Bit (WOB) and excitation parameters.

Prediction and optimization of drilling rate of penetration has been the center of numerous research works for a long time in the drilling industry. The perfect hole cleaning model by Maurer in 1962 [29] is one of the oldest and the most widely used models to predict the Rate of Penetration (ROP) as a function of Weight On Bit (WOB), rotary speed, formation strength and bit diameter. Apart from this, other researches have also produced models to predict ROP [30] and Mechanical Specific Energy (MSE) [31] or Hydromechanical Specific Energy (HMSE) [32]. The goal of all these research works is to enable the driller to predict effects of various drilling parameters on the ROP and optimize them for increasing the drilling efficiency.

With the goal of optimizing the drilling performance, a stream of research is focused in harnessing the vibration to improve the ROP. As a part of ongoing research, the study of vibration assisted rotary drilling has been one of the major focuses at the Drilling Technology Laboratory (DTL) of Memorial University of Newfoundland (MUN). In an experimental study by Li et al. [33] variation in vibration amplitude was found to be a significant factor in increasing the ROP using a coring bit. Similarly, Babatunde et al. 2011 [34] carried the work forward by investigating the effect of changing frequency and amplitude of vibration. Both of these experiments used an electromechanical axial shaker mounted at the bottom of the drill stand as the source of active vibration and demonstrated impact of vibration in enhancing the drilling performance.

In another set of experiments performed by Babatunde et al. 2011 [34], the effect of change of vibration parameters was studied on a diamond drag bit which showed significant increase in ROP at controlled frequencies. Experiments with Polycrystalline Diamond Compact (PDC) bits show

that with the compliance tool low WOB cannot produce a drastic improvement in the ROP as the main bit cutter face cannot partake in penetration process [35]. One of the hypotheses that has been proposed in this research is that axial compliance in the drill string creates the bit rock displacement which reduces the cuttings accumulation in the zone of penetration thus optimizing bottom hole cleaning [35].

Numerous lab and field scale experimental works with the p-VARD tool have demonstrated improvements in the drilling performance. In a recent experimental work involving the p-VARD tool, Molgaard et al. [28] reported a significant increase in DDWOB with the use of p-VARD tool. The experiments involved drilling holes parallel to shale bedding on specimens of equal height using a dual cutter PDC and diamond impregnated coring bit. The DDWOB is the WOB measured by the load cell placed below the drilling specimen.

This work focuses on development and analysis of bond graph model of p-VARD tool. The numerical model developed with the help of the bond graph enables us to see the relationships between different parameters and guide us towards how to best optimize them for enhancing the drilling performance. A comparative study has been performed to illustrate how the use of p-VARD tool dampens the vibration at the drill rig while optimizing the DDWOB.

4.2. Modeling of Drilling System

The drilling system analyzed in this chapter is a Small Drilling Simulator (SDS) at DTL, MUN. The details on this drilling system have been published in many papers including Khorshidian et al. 2014 [36], Shah et. al. 2019 [27] and Rana et. al. 2015 [24]. The rotary unit of the SDS is run by a Milwawkee motor which delivers 80 Nm torque at 300 rpm and 40 Nm torque at 600 rpm.

Similarly, the fluid circulation system has a triplex pump with maximum flow capacity of 150 L/min at 6,900 kPa and the WOB is applied by the suspended plates using rack and pinion mechanism [24]. The SDS comes with variety of instrumentation to measure the axial movement, rotary speeds and downhole WOB. Figure 27 shows the SDS with labels showing its different components and instruments.
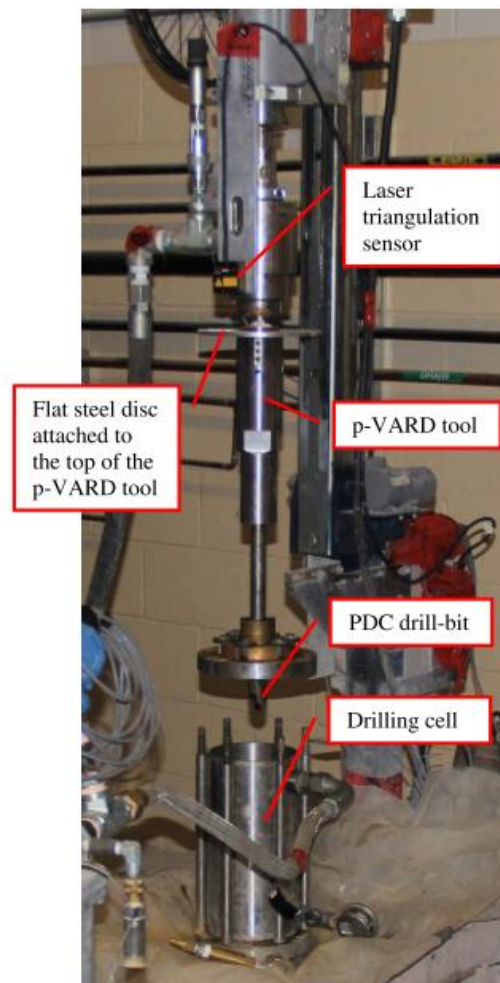
Figure 27: Showing different components and instruments of SDS [24]

For simplicity, the sub-components of SDS that are included in the bond graph modeling are WOB, drill string/bottom hole assembly, formation stiffness and bit-rock interaction along with the p-VARD tool. These sub-components make up the compliant and the stiff drilling system when operated with and without the p-VARD tool. Figure 28 represents a schematic of the stiff drilling system, whereas Figure 29, with an addition of p-VARD tool, represents a compliant drilling system, where the individual p-VARD rubber elements are represented with an equivalent damping.
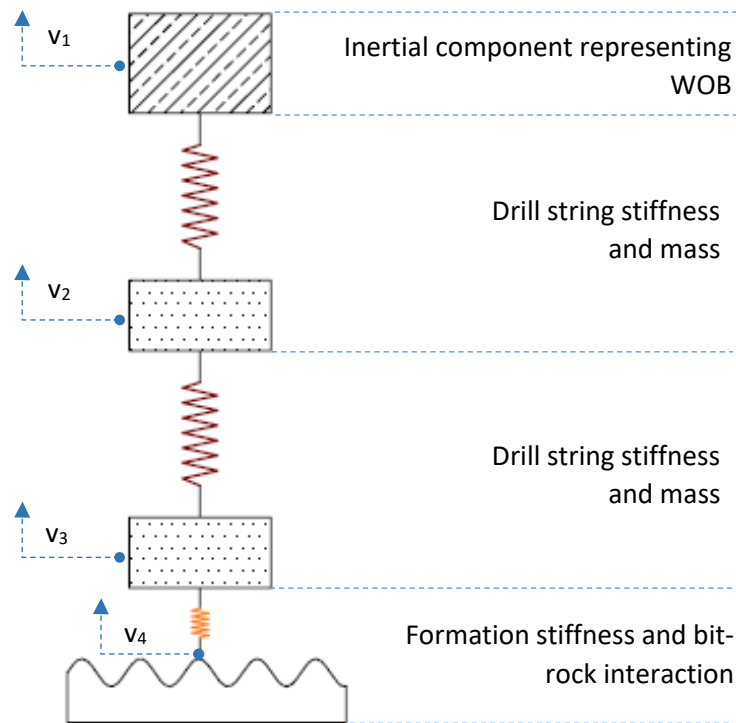
Figure 28: Schematic of stiff drilling system

4.2.1. Weight on Bit

SDS transfers WOB from the suspended plates to the formation with the help of a rack and pinion mechanism. Additionally, WOB is generated by the weights of the mechanism, drill motor and swivel, which sits on the top of the drill string. For this reason, the WOB considered for the simulation is the weight of all these components combined, which is represented by a single inertial
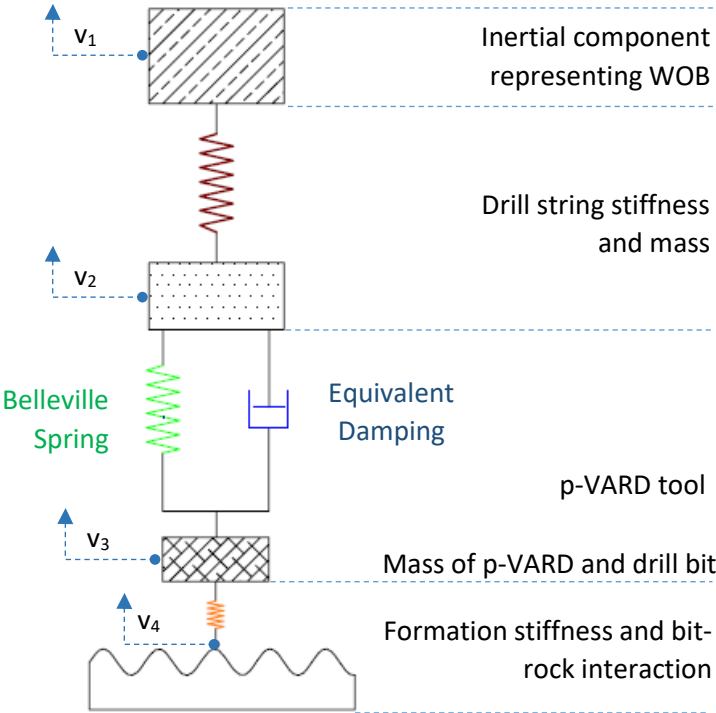
Figure 29: Schematic of drilling system with p-VARD

component in the schematic diagram. A general representation of the weight on bit that is applied to the systems is given by below equation, and is plotted in Figure 30.

$$WOB(kN) = a + b \times number\ of\ plates\ (n)$$

$$where\ a = 0.8313, b = 0.1487$$
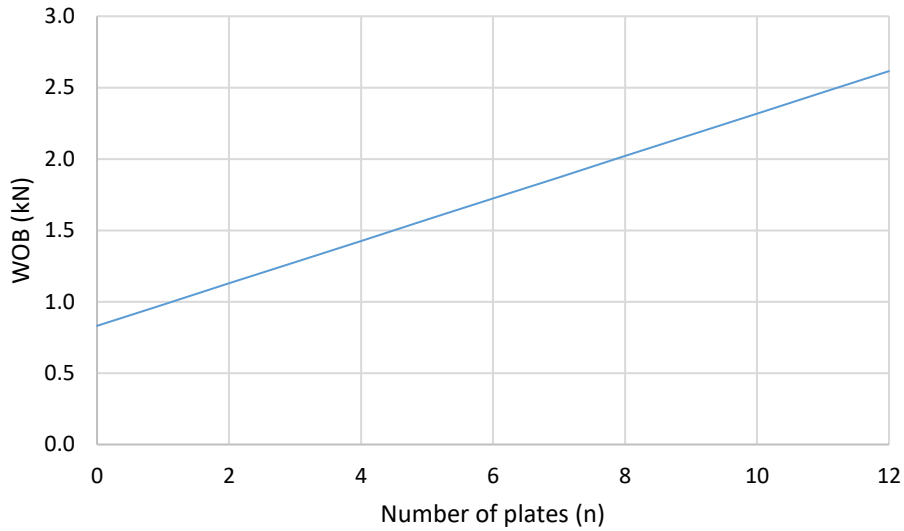
Figure 30: WOB applied through SDS

4.2.2. Drill String

Drill string (DS) connects the SDS swivel to the drill bit and transfers torque, WOB and drilling fluid. A lumped parameter model of DS for axial motion is used to define the governing equations and it comprises of following parameters [11]:

$$Stiffness\ (k) = \frac{AE}{l}, \qquad\qquad \text{................................. (viii)}$$

$$Mass\ (m) = \frac{mass\ of\ DS}{3} \qquad\qquad \text{................................. (ix)}$$

Where, A is DS cross sectional area, E is Young's Modulus and l is length of the DS

45

In addition to the stiffness, the DS is modelled with a damping ratio of $\zeta = 0.01$, which is the standard value for small diameter steel pipes [37]. For this study, a 1 inch outer diameter (OD), 0.75 inch inner diameter (ID), 12 inch long DS is used.

4.2.3. p-VARD tool

This tool provides axial compliance and dampening to the vibration generated by the top drive system and the bit-rock interaction, while functioning as a part of the drill string. Detailed explanation on various components of a p-VARD tool in context of LDS is given in Chapter 6. In the schematics of Figure 29, the p-VARD tool is represented as a parallel combination of Belleville springs and rubbers, whose characteristic properties are explained in following sections.

i.   Belleville springs

The p-VARD tool uses Belleville springs as an energy storage device. High strength and flexible compliance make these springs suitable for the p-VARD tool. Although many researches have been done to plot the load-deflection characteristics of these springs, the first equation proposed by Almen-Laszlo [13] is used for the purpose of this research because of its simplicity.

The unique nature of the Belleville spring stack make it necessary to model this component as a conditional compliant element. When the spring is fully compressed, it becomes as stiff as the DS and when it is relaxed beyond the uncompressed free height, it doesn't exert any pulling force. A systematic way to code this into the bond graph C-element has been explained in Section 3.1.

Below equations, as proposed by Almen-Laszlo [13] are used to govern the load-deflection relation of the Belleville spring stack:

$$P = JP_m \qquad \qquad \dots\dots\dots\dots\dots\dots\dots\dots\dots \text{ (v)}$$

$$\text{where } P_m = \frac{E\bar{\delta}}{(1-\vartheta^2)\,r_2{}^2}\left[(h-\bar{\delta})\left(h-\frac{\bar{\delta}}{2}\right)\frac{t}{M}+\frac{t^3}{N}\right] \qquad \dots\dots\dots\dots\dots\dots\dots\dots \text{ (vi)}$$

$$\frac{1}{M} = \left[\frac{\gamma+1}{\gamma-1}-\frac{2}{\ln\gamma}\right]\pi\left(\frac{\gamma}{\gamma-1}\right)^2$$

$$\frac{1}{N} = \frac{\pi}{6}\ln\gamma\left(\frac{\gamma}{\gamma-1}\right)^2$$

$$\gamma = \frac{r_2}{r_1}, \qquad \bar{\delta} = \frac{\delta}{I}$$

Detail explanation to these parameters are given in Chapter 2. For the purpose of this study, a spring with 0.755 inch ID, 1.5 inch OD, 0.045 inch thickness (t) and 0.093 inch height (H) is chosen. The specification of this spring can be found under McMASTER reference number 9712K86 [38].

   ii.   Rubber elements

The rubbers used in the p-VARD tool serve the purpose of dampening the vibrations. Schematically, they are connected in parallel to the Belleville springs, but intrinsically, they are each composed of ideal spring and damper connected in parallel (see Figure 29).

An empirical relation can be established through a series of experiments to relate the stiffness and dampening coefficients of the rubbers to a range of excitation frequency and amplitudes. One such work performed by Zhong 2015 [39] produces equations for the stiffness and damping coefficients of field scale p-VARD rubbers, which are 2.1 inch ID, 4.75 inch OD & 0.5 inch thick Buna-N, also known as acrylonitrile butadiene rubber. These material properties are responsible for inherent

stiffness of the rubber rings in addition to its damping, which is very challenging to model numerically. A series of experiments done by Zhong 2015 [39] derived such empirical equations relating the rubber stiffness and damping to excitation frequencies and amplitudes as follows:

$$k_{rubber} = 0.43a^2f^2 - 9.22a^2f - 0.19af^2 + 45.75a^2 - 10.57a - 1.59f^2 + 43.87f - 224.7 \quad ......(x)$$

$$c_{rubber} = 0.02a^2f^2 - 1.45a^2f + 0.15af^2 + 40.45a^2 - 90.09a - 0.70f^2 + 14.63f - 3.95 \quad .....(xi)$$

Where, k_{rubber} is the rubber stiffness coefficient in kN/mm

c_{rubber} is the rubber damping coefficient Ns/mm

a is the amplitude of vibration in mm

f is the frequency of vibration in Hz

On the other hand, the lab scale p-VARD tool uses 1.5 inch ID, 2.3 inch OD & 0.25 inch thick neoprene rubbers with moderate damping ratio (ζ) of 0.05 [40] thus producing an underdamped system response. These rubbers have very low or almost no stiffness and the closed cell characteristics of this material makes it suitable for using in lubricated environment. For the purpose of this study, the lab scale p-VARD rubbers elements are assumed to be ideal dampers with negligible stiffness. The following set of equations is used to determine the damping coefficient (b) of the rubber stack.

$$\zeta = \frac{damping\ coefficient}{critical\ damping\ coefficient} = \frac{b}{2\sqrt{k\ m}} \qquad .... (xii)$$

where, k and m are equivalent stiffness and mass of the drill string model

A series connection of n number of these rubbers would result in equivalent damping coefficient of b/n, which is input into the bond graph model to represent the rubber damping.

4.2.4. Bit-rock interaction

Bit rock interaction is reviewed in the literature as being a critical input for drill string vibration analysis. In the modeling field, bit-rock interaction stands as a rather complex problem because the exact solution is very complicated to represent mathematically as they are formulated by delay differential equations. It is possible to model the rock axial forces as a spring-damper system that is dependent on formation properties and the system parameters like ROP and WOB. The numerical model representing bit-rock interaction includes the displacement component due to lifting action of the bit which is sinusoidal and with a frequency component which corresponds to the type of bit used [41].

For the purpose of this study, bit-rock interaction is represented by a sinusoidal wave with frequency equal to the frequency of rotation and different amplitude ranges. 20-sim parameter sweep is used to find the parametric effect of frequency and amplitude on the total system response. In the bond graphs, (Figure 31 and Figure 32) bit rock interaction generates a sinusoidal displacement source at the bit-rock interface, which is differentiated and input into rest of the system.

4.3. Bond Graph Generation

Based on the premises developed in Section 4.2, bond graphs are developed for the rigid and the compliant drilling systems with following parameters.

Table 2: Parameters of drill string system

Parameters		Units	Values
WOB	Weight	*kN*	*a+b×n*
Drill String	Length	*inch*	*12*
	ID	*inch*	*0.75*
	OD	*inch*	*1*
	Mass	*kg*	*0.58*
p-VARD tool	Spring — ID	*inch*	*0.755*
	Spring — OD	*inch*	*1.50*
	Spring — Thickness	*inch*	*0.045*
	Spring — Height	*inch*	*0.093*
	Rubber — Damping ratio (ζ)	-	*0.05 – 1.00*
	Rubber — Damping coefficient	*Ns/m*	$2\,\zeta\,\sqrt{k\,m}$
	Rubber — Number of rubbers	-	*3*
	Mass	*kg*	*10*
Bit Rock interaction	Frequency	*rpm*	*0 - 600*
	Amplitude	*mm*	*0.5 - 2*

The bond graphs for the rigid and the compliant drilling system are shown in Figure 31 and Figure 32 respectively. In the bond graph, the sinusoidal displacement function is differentiated and input into the system as the velocity input at the bit/rock contact point ($v5$). The p-VARD tool in Figure 32 is shown as a parallel combination of Belleville spring stack and rubber stack, which is then

connected to the drill string in series. The drill string in Figure 31 and Figure 32 is represented by a stiff spring with low damping and a one-third lumped mass. Similarly, the velocity $v1$ of top inertial component is then integrated to observe the top displacement. The weights of all inertial components make up for the sources of efforts (Se) due to the gravity, which are joint at their corresponding ports. The bond graphs have been constructed with some additional features like differentiator, integrator and minimum/maximum sensors to aid in result analysis. Additionally, parasitic damping have been added together with the springs to avoid any causality errors.
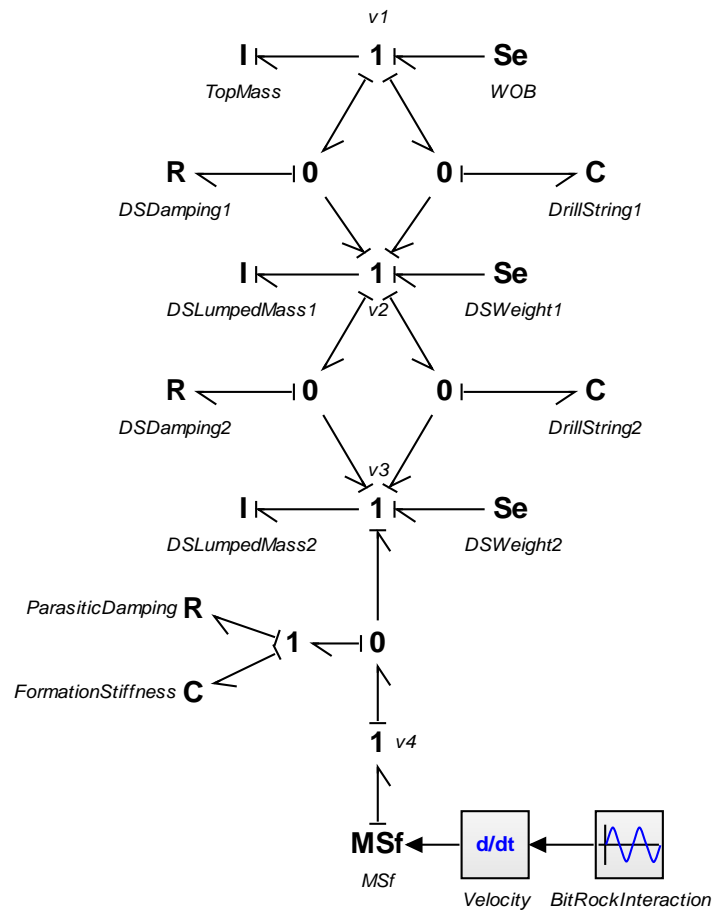
Figure 31: Bond graph model of a stiff drilling system

Figure 32: Bond graph model of a compliant drilling system

4.4. Results

In this section, system parameters are varied, and their effects are observed. The primary effect of the p-VARD tool has been seen in softening the drill string and lowering its natural frequency. This can make the drill string resonate at lower workable ranges of frequencies comparable to typical drilling speeds. Similarly, another effect of p-VARD tool has been seen in the attenuation of excessive vibration particularly at frequencies higher than its natural frequency. In this section, system variables like damping ratio, excitation amplitude, compliance and WOB are plotted against the frequency of excitation followed by discussion and conclusion in Section 4.5.

4.4.1. Effect of Damping ratio(ζ)

The damping ratio of the p-VARD tool is 0.05, a standard value for Neoprene rubbers. This means that in one cycle, 5% of energy is dissipated by the system. To examine the effect of the damping ratio, its value is gradually increased from the underdamped condition of $\zeta = 0.05$ to critically damped condition of $\zeta = 1$ and the effects are observed. Figure 33 shows that the uncontrolled motion produced by the system resonance can be reduced by increasing the damping ratio and as the system approaches critical damping, the vibration amplification due to resonance becomes significantly low.
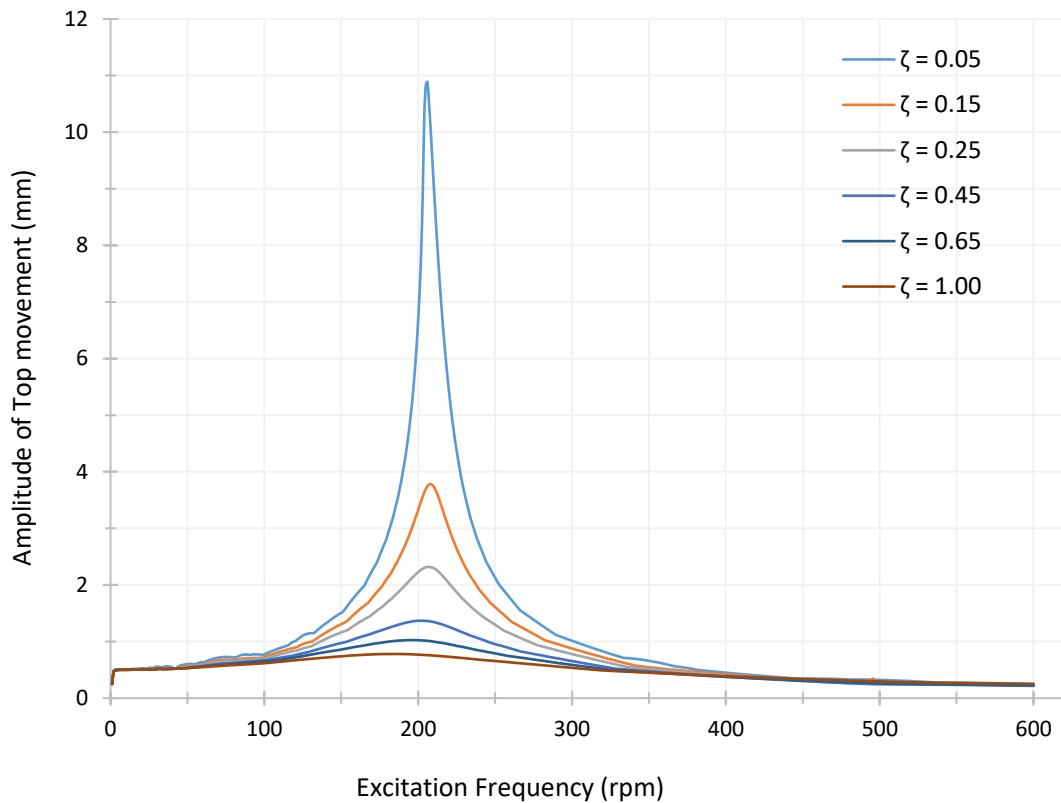
Figure 33: Showing the effect of damping ratio [System parameters: I = 20, J = 1, a = 0.5mm]

4.4.2. Effect of excitation amplitude

To observe the effect of the excitation amplitude, the damping ratio is set to 15% and the amplitude of vibration is gradually increased from 0.1 mm to 1.4 mm. These parameters are selected because as the excitation frequency approaches the natural frequency of the system, the stack of Belleville springs tend to compress more frequently, and this phenomenon is more likely as amplitude of excitation increases. This limits the upper bound of excitation amplitude for a combination of spring configuration and damping ratio. One way to prevent the flattening of Belleville springs is to increase the damping ratio of the p-VARD tool as shown in Figure 33. As can be seen from Figure

34, the amplitude of excitation does not alter the range of system resonance, rather it scales up the magnitude of displacement of top mass. It is also observed that at amplitudes greater than 1.4 mm, the Belleville springs become flat which instantaneously makes them stiff and stops the resonance.
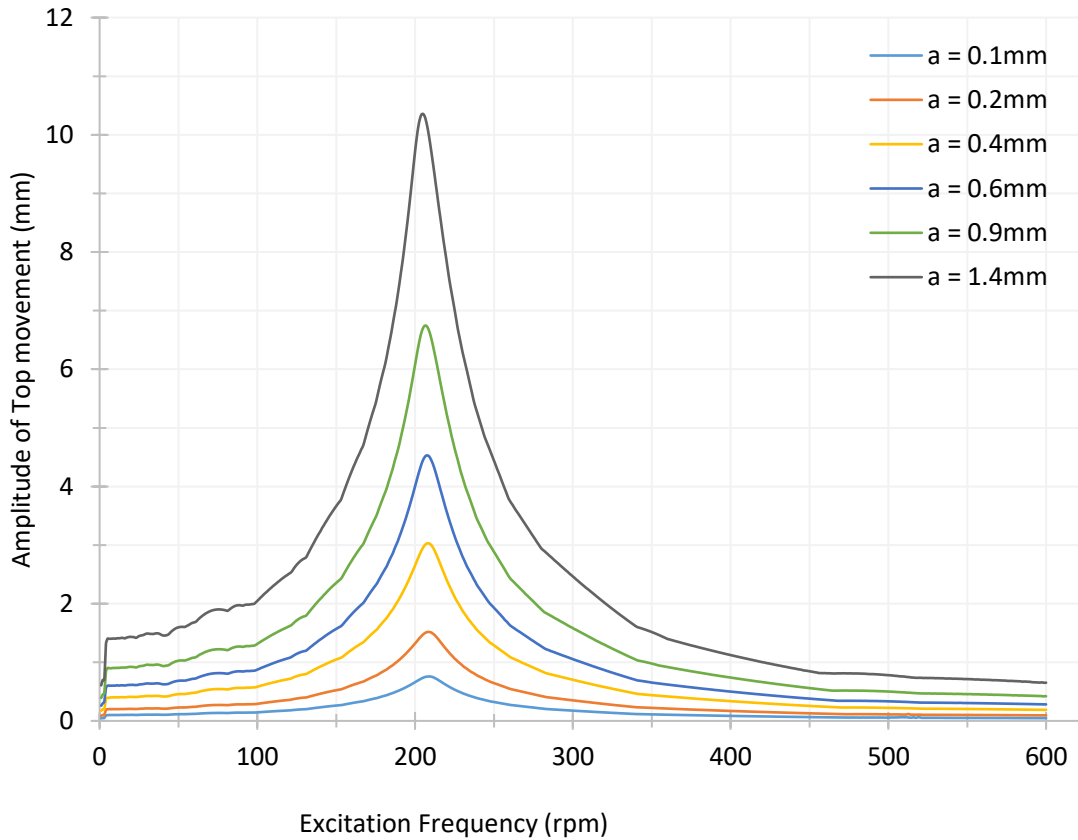
Figure 34: Showing the effect of excitation amplitude [System parameters: I = 20, J = 1, ζ = 0.15]

4.4.3. Effect of p-VARD compliance

The compliance of the p-VARD tool is altered by increasing/decreasing the number of springs in series (I) and parallel (J) (refer to Section 2.3.2 for more details). Increasing number of springs in series makes the springs more compliant while increasing number of springs in parallel makes

them stiffer. As shown in Figure 35, it is observed that the resonating frequency of the system increases with the increase in p-VARD stiffness, which is justifiable as the natural frequency is directly proportional to the square root of the system stiffness. Also, because the p-VARD stiffness is less compared to that of the drill string, it can be assumed to be representative of the system stiffness.
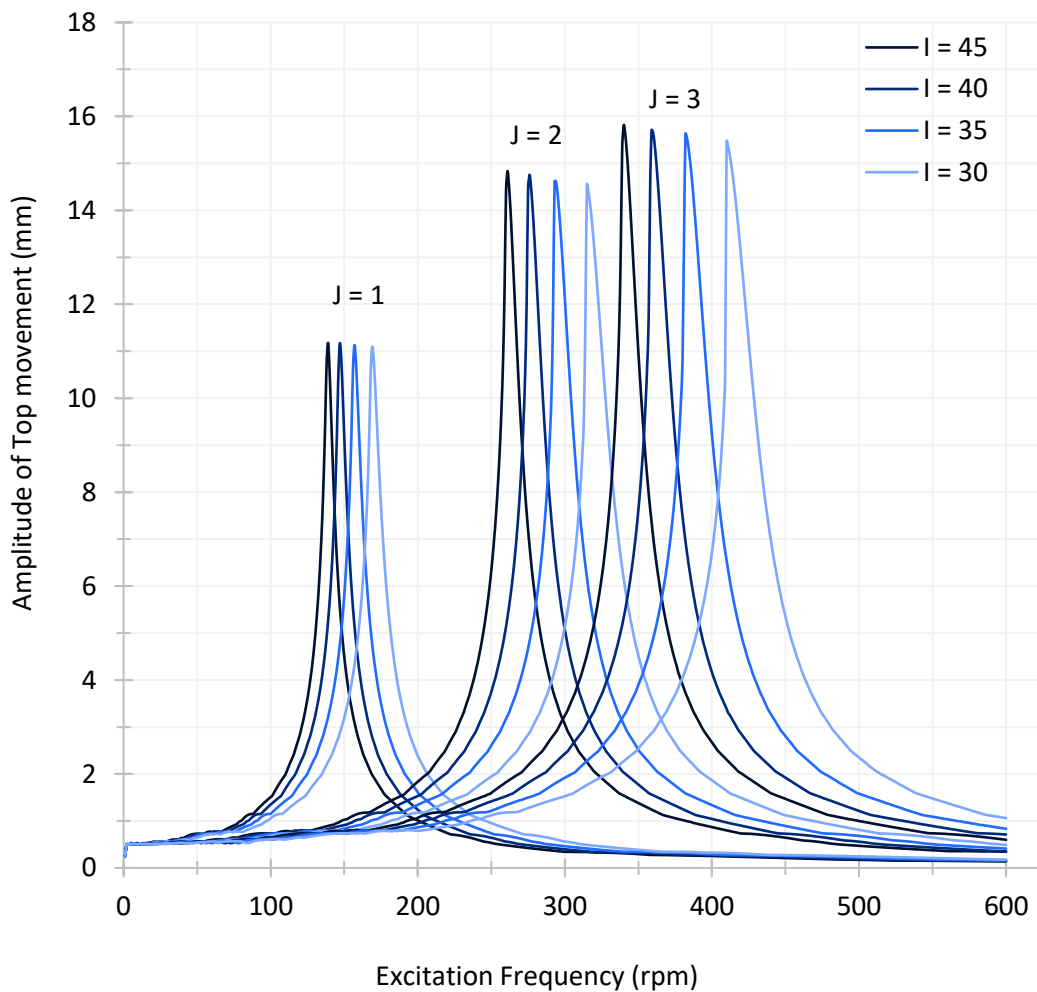
Figure 35: Showing the effect of spring compliance
[System parameters: ζ = 0.15, excitation amplitude = 0.5 mm]

4.4.4. Effect of the Top Mass[WOB]

The resonating frequency of a mass-spring-damper system is inversely proportional to the square root of the sprung mass, which in this case is primarily represented by the top mass, the gravitational force of which produces WOB of the system. The value of WOB is gradually increased by increasing the number of plates (n) and the system response over the range of operating frequency is plotted. Figure 36 shows that there is a co-relation between the WOB and the resonating frequency, i.e. the system resonates at lower frequency as the WOB is increased.
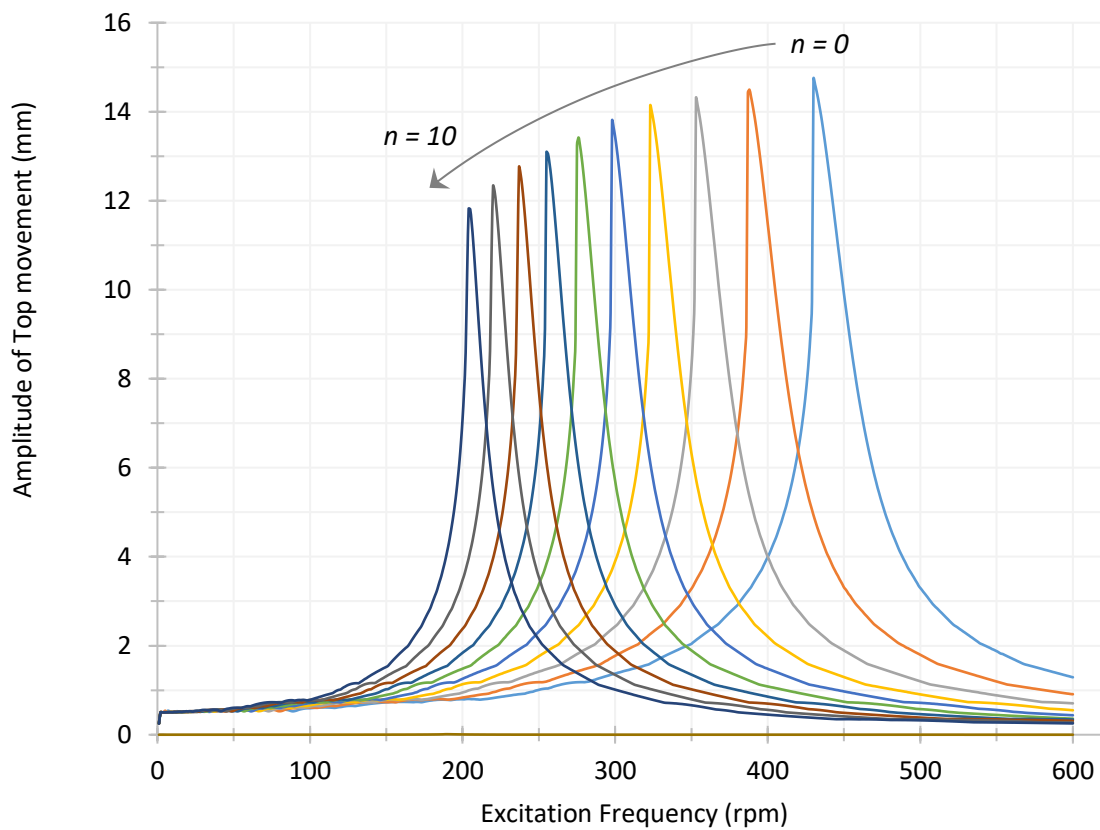
Figure 36: Showing the effect of WOB [System parameters: I = 25,
J = 2, ζ = 0.15, excitation amplitude = 0.5 mm]

4.5. Discussion and Conclusion

As seen from simulation results of Section 4.4, it is observed that adding a p-VARD tool to the drill string makes the whole system more compliant bringing the resonating frequency to a workable range. The system resonating frequency for a linear mass-spring-damper model of a rigid drill string system is at the range of 900 rad/sec or 9000 rpm while adding a p-VARD tool in series with the drill string can lower this frequency to the workable range of 300 rpm.

A study of the influence of system parameters of a compliant drilling system shows that spring configuration and weight on bit can alter the natural frequency of the drilling system. The lower the spring compliance, the higher is the resonating frequency and the higher the weight on bit, the lower is the resonating frequency. This can be observed from Figure 35 and Figure 36. In Figure 35, as the system becomes stiffer with more springs in parallel, the resonating frequency increases accordingly and as it becomes more compliant with more springs in series, the resonating frequency decreases. Similarly, in Figure 36 as the WOB is increased by increasing the number of plates, the system resonates at lower frequency. With reference to this plot, an operator can make the drill string resonate at desired frequency by altering the number of plates for a given configuration of Belleville springs, rubbers, drill string and rotary speed.

Similarly, damping ratio of the rubber elements plays a critical role in attenuating the vibration. The damping ratio should be properly calibrated to prevent the flattening of Belleville springs, especially at around the system resonating frequency. Although the results due to insufficient damping are not included in this work, it will cause flattening of the springs and terminate the resonance prematurely. Of all, amplitude of excitation does not have significant effect in defining the nature of system response rather it only scales up or down the magnitude of vibration and does

not alter the system natural frequency. However, higher amplitudes near the system natural frequency may cause flattening of springs.

Figure 35 and Figure 36 show that the system can resonate successfully at 300 rpm for different combination of system parameters. Similarly, this modeling can help in predicting the flattening of the Belleville springs due to high weight on bit or high excitation frequency. In this scenario, the stiffness of the system rises abruptly and reaches close to that of the drill string, which then stops the system excitation as the system natural frequency increases. A strategic design of experiment should avoid this phenomenon and let the system oscillate without flattening the springs. Also, flattening of Belleville springs may cause failure of torque transmitting keys and the outer shell of the p-VARD tool. However, care should be given to minimize the fatigue load generated by the high excitation amplitudes due to system resonance. This trade-off between system oscillation and its fatigue life can be modelled and incorporated into the design of experiment, which can be a future work.

The relation between system parameters is consistent with that of a linear spring but use of bond graphs makes it easy to model the complicated load-deflection relationship of the Belleville spring. As an improvement to this work, modeling of frictional losses in Belleville springs can be done to understand the effect of spring lubrication and surface finishes.

Chapter 5   Modeling Frictional Losses in Belleville Springs

This chapter is based upon the paper titled *"Calculating Frictional Losses in Belleville Springs by Linear Interpolation"*, which has been published at the ASME 39th International Conference on *Ocean, Offshore and Artic Engineering 2020*. This paper is co-authored with Shaheen Shah, Dr. Abdelsalam Abugharara and Dr. Stephen Butt.

5.1. Introduction

In this chapter, a new approach of linear interpolation is used to calculate the relative displacements that takes place in the springs during its loading and unloading cycle. Because of relative movement of spring with respect to supporting surfaces and the mating spring surfaces, frictional losses in the spring take place during each compression and relaxation cycle leading to a slightly different load-deflection curve from what has been defined in the literature. The geometry of the spring combined with different stacking configurations complicate the study of frictional losses in these kinds of springs.

Although much work has been done in the field of Belleville springs, study of effect of friction in Belleville springs is very limited. Curti and Montanini [17] in their approach to generate more accurate spring characteristics studied the effect of friction between spring edge and the supporting surface. The theoretical formulation was verified by comparing the results with that from the FEA. However, their work was limited to the study of friction between the spring and supporting surfaces only. This limited the implementation of this work as Belleville springs are always stacked in series, parallel or the combination of both.

In a work by Ozaki et. al. [23], in addition to the edge friction between the spring and the supporting surfaces, the surface friction that exists between the mating surfaces of two or more parallelly stacked springs was also incorporated. The authors have shown a comparison between Almen-Laszlo's equation and the results from the FEA which clearly show the missing frictional component in Almen-Laszlo's equation during loading and unloading of the springs, thus highlighting the need of more research in this field. They use a link type connection that neglects the spring rotational moment to calculate the displacement of spring edge with respect to the supporting surface and the displacement of spring surfaces stacked in parallel. The hysterics loss during one spring cycle is then calculated in parts as a summation of frictional loss at the edges and that on the spring surfaces. The work further extends to formulate a generic equation which can be used to determine the hysterics losses during loading and unloading of the springs.

This work presents a new method to calculate the displacement of different points of Belleville springs during its loading and unloading using linear interpolation method. The results of spring displacement are then used to develop a model to calculate frictional load as a function of spring deflection, which is used to analyse load-deflection curves of springs with different dimensional and frictional parameters. The developed methodology is used to plot and understand characteristics curves of four different kind of Belleville springs; High Load, Standard, Force Limiting and Force Adjusting Belleville springs by plotting the graphs for different free-height to thickness and diameter ratios. In the later section, the proposed methodology has been used to visualize the load-deflection characteristics of Belleville springs used in the p-VARD tool of the Large Drilling Simulator, one of the state-of-the-art drilling simulators at Memorial University of Newfoundland. Results show that understanding of the characteristic curves of different spring

61

configuration helps to plan to drill with desired WOB using a p-VARD tool.Design parameters of Belleville springs.

5.2. Method of Linear Interpolation

Interpolation helps us connect the dots between two specified points. Principle of linear interpolation implies that if the co-ordinates of two points in XY plane are $A\ (x_1, y_1)\ \&\ B\ (x_2, y_2)$ then any point $C\ (x, y)$ that lies on the straight line AB can be determined by interpolation as shown in Figure 37.

$$\frac{y - y_1}{x - x_1} = \frac{y_2 - y_1}{x_2 - x_1}$$
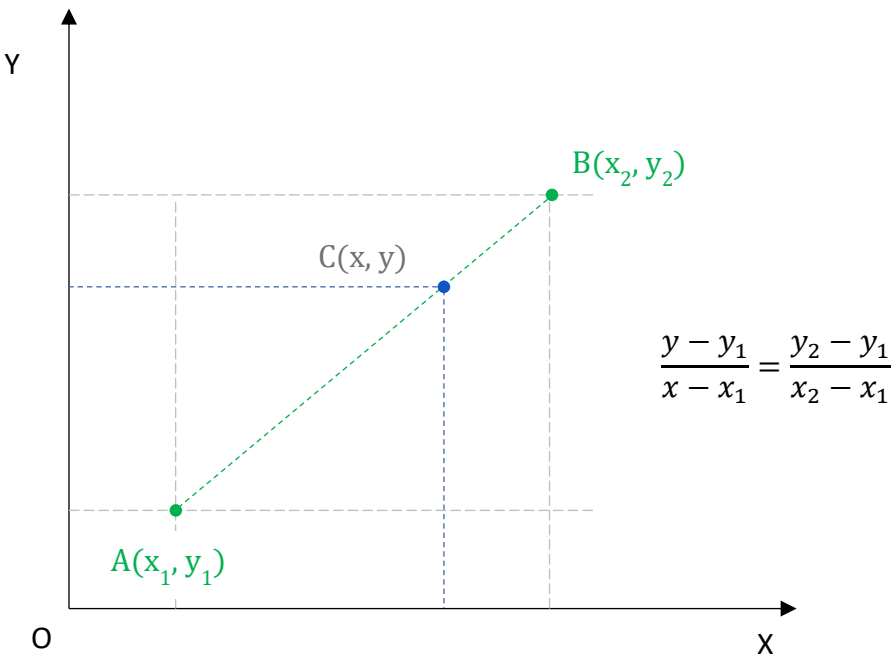
The edge displacement is observed at the point of contact between the spring and the supporting surface and the surface displacement is observed between two springs stacked in parallel. Frictional losses take place at these sliding surfaces and can be estimated if these displacements are known.

In this work, linear interpolation is used to determine the intermediate values of edge displacement and surface displacement when the Belleville spring are compressed/relaxed. Two points of zero deflection and maximum deflection are taken as the initial and the final point. At zero deflection, both deflection and edge/surface displacements are zero and at the maximum deflection, the deflection and edge/surface displacements can be calculated from the spring geometry. Thus, using the principle of linear interpolation, edge/surface displacements can be expressed as a function of spring deflection. These displacement values are later used to calculate the frictional losses in the springs.

5.3. Calculating the Edge displacement

This section describes the proposed methodology to calculate the displacement of spring edge with respect to the supporting surface. The derivations here are based upon the fundamental assumptions of Almen-Laszlo's work, i.e. the cross-section of the spring doesn't deform but rather rotates about a neutral point when it is deformed, where the neutral point is the midpoint of the diagonal of the spring cross-section.

Let us consider a spring, which is being compressed in its axial direction as shown in Figure 38.

Here O is the neutral point of the spring about which the spring cross-section rotates, when it is deformed. The spring has the inner radius r_1 and outer radius r_2 with t thickness and H total height.

With reference to Figure 38, we can express the spring angle $\emptyset$ in terms of spring parameters. If we refer to $\Delta\,ADG$,

$$\tan\emptyset = \frac{DG}{AG} = \frac{GD' - DD'}{r_2 - r_1 - AB'} = \frac{H - BB'}{r_2 - r_1 - AB'} \qquad \text{...............................} (xiii)$$

From Δ ABB', we can get the equations of BB' and AB' in terms of spring parameters.

$$\cos \emptyset = \frac{BB'}{AB} = \frac{BB'}{t} \qquad \text{................................. (xiv)}$$
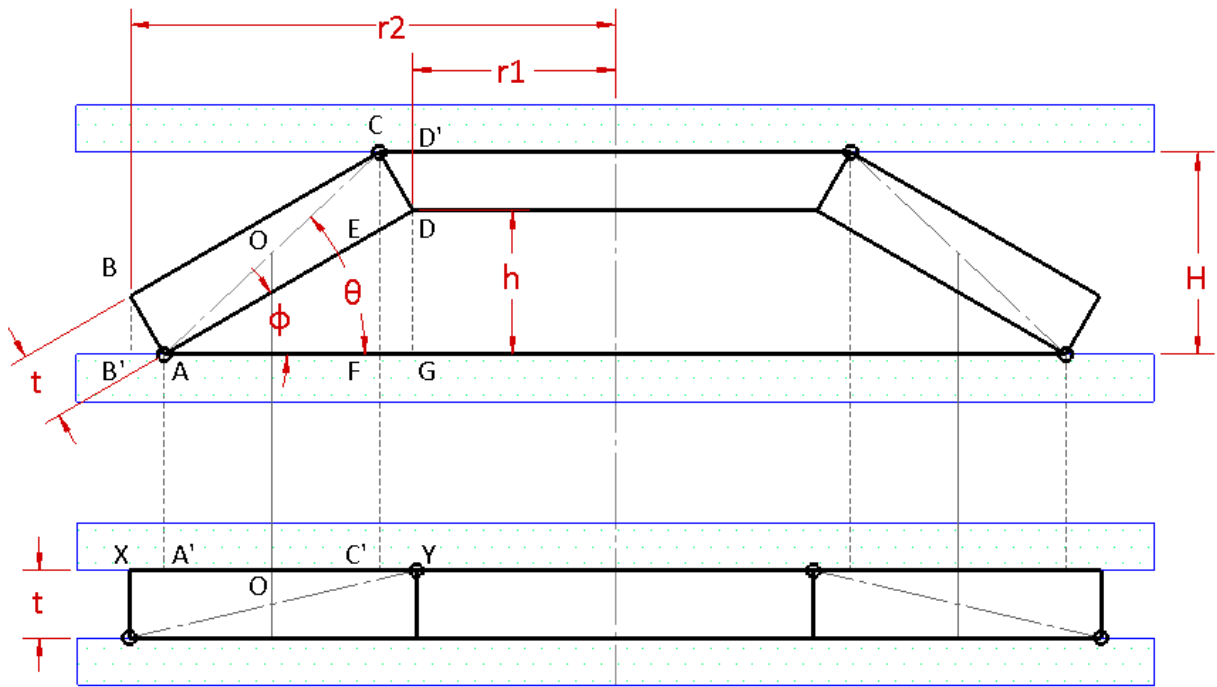
Figure 38: Illustration of edge displacement in Belleville spring

$or, BB' = t \cos \emptyset$

Similarly,

$$\sin \emptyset = \frac{AB'}{AB} = \frac{AB'}{t}$$

$or, AB' = t \, \sin \emptyset \qquad \text{................................. (xv)}$

Substituting the values of BB' and AB', we get the equation for $\tan\emptyset$ as:

$$\tan\emptyset = \frac{H - t\cos\emptyset}{r_2 - r_1 - t\sin\emptyset} \qquad\qquad\text{............................... (xvi)}$$

Next, the free height of the spring is determined as:

$$h = DG = GD' - DD' = GD' - BB'$$

$$or, h = H - t\cos\emptyset \qquad\qquad\text{............................... (xvii)}$$

In Figure 38, the edge displacement has been shown with two small circles. The edge displacement at the top point C is equal to the edge displacement at the bottom point A but are in opposite direction. We can derive the equations for the edge displacement, by referring to the projection of uncompressed spring on the fully compressed spring. The lower diagram in Figure 38 shows a fully compressed spring where the edge displacements are maximum.

From the geometry of the spring, we can determine that

$$edge\ displacement\ (u_e) = XA' = YC' = \frac{XY - A'C'}{2} = \frac{AD - AF}{2}$$

From $\Delta\ ACD$,

$$\tan(\theta - \emptyset) = \frac{CD}{AD}$$

$$or, AD = \frac{t}{\tan(\theta - \emptyset)}$$

And, $AF = r_2 - r_1 - AB' - CD' = r_2 - r_1 - 2\ t\sin\emptyset$

Substituting these values, we get the equation for edge displacement as:

$$u_e = \frac{\dfrac{t}{\tan(\theta - \emptyset)} - r_2 + r_1 + 2\,t\,\sin\emptyset}{2}$$ .... (xviii)

We can also derive the equation for the neutral line angle θ in terms of spring parameters. If we refer to $\Delta\,ACF$,

$$\tan\theta = \frac{CF}{AF} = \frac{H}{r_2 - r_1 - 2\,t\,\sin\emptyset}$$

$$or,\,\theta = \tan^{-1}\frac{H}{r_2 - r_1 - 2t\,\sin\emptyset}$$ .... (xix)

The two initial and final points necessary for the process of interpolation have been defined by now and they have been successfully expressed in terms of spring parameters. The next step after determining the initial and the final condition is to interpolate the values of edge displacement as a function of spring deflection (δ). In the table below, the concept of linear interpolation has been implemented to express the edge displacement as a function of axial deflection.

Table 3: Interpolation table for calculating intermediate edge displacement

	Initial point	Final point	Intermediate points
Deflection	0	$h = H - t\cos\emptyset$	δ
Edge Displacement (u_e)	0	$\dfrac{\dfrac{t}{\tan(\theta - \emptyset)} - r_2 + r_1 + 2\tan\emptyset}{2}$	$\delta \times \dfrac{u_{e\_final}}{h}$

5.4. Calculating the Surface Displacement

To derive the equation for the surface displacement, let us consider the deflection phenomenon of $I = 1, J = 2$ configuration of Belleville springs as shown in Figure 39. The lower part of the diagram shows fully flattened springs when the surface displacement is maximum. From the study of the diagram, it can be found out that the maximum surface displacement that takes place between two springs mated in parallel is:

$$u_s = BC = AB \sin \emptyset = t \sin \emptyset$$
$$\dots\dots\dots\dots\dots\dots\dots\dots\dots (xx)$$

Implementing the approach of linear interpolating, we can determine the value of surface displacement (u_s) for all intermediate values of spring deflection (δ) as shown in Table 4.

Table 4: Interpolation table for calculating intermediate surface displacement

	Initial point	Final point	Intermediate points
Deflection	0	$h = H - t \cos \emptyset$	δ
Surface Displacement (u_s)	0	$t \sin \emptyset$	$t \sin \emptyset \times \left(\dfrac{\delta}{H - t \cos \emptyset} \right)$
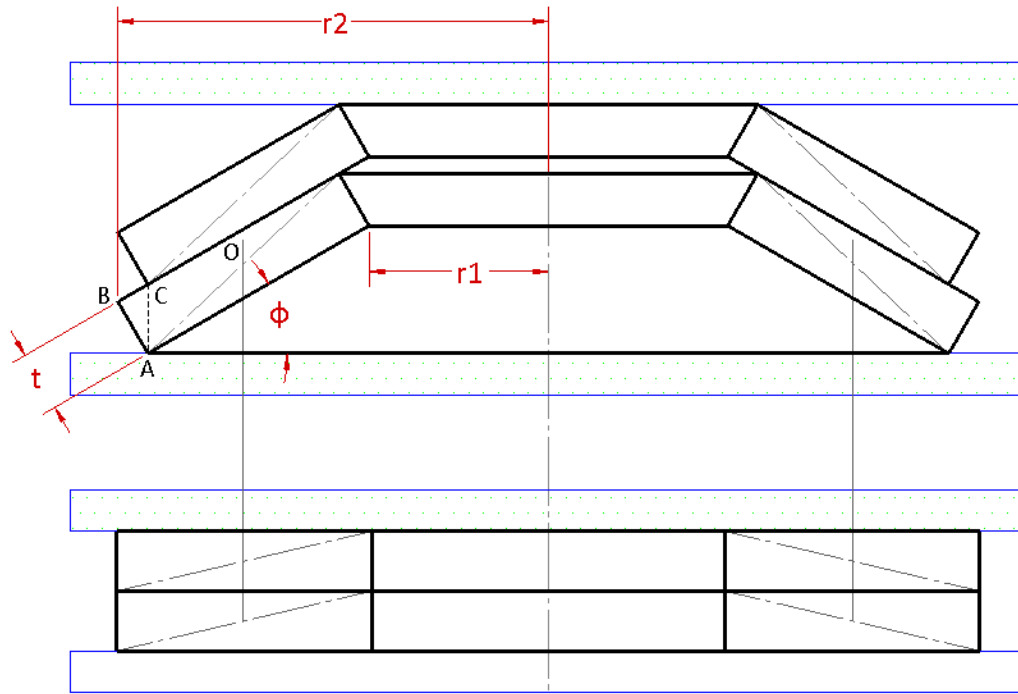
Figure 39: Illustration of surface displacement in Belleville springs

5.5. Effect of friction in Load-Deflection curve

After we have derived the equations for the edge/surface displacements in terms of instantaneous spring deflection, our next goal is to determine the frictional dissipation during the loading and unloading of the spring. Following the methodology proposed by Ozaki et. al. [23], frictional dissipation is calculated as product of frictional force and corresponding displacement, which can then be converted to equivalent load increment by dividing by the equivalent displacement. Thus, corrected load-deflection curve for the Belleville spring as proposed by Ozaki et. al. [23] can be used which undertakes the effect of frictional losses as follows:

$$P = JP_m + \Delta P \qquad\qquad\qquad \text{............ (xxi)}$$

$$where, P_m = \frac{E\bar{\delta}}{(1 - \vartheta^2)\, r_2{}^2}\left[(h - \bar{\delta})\left(h - \frac{\bar{\delta}}{2}\right)\frac{t}{M} + \frac{t^3}{N}\right] \qquad\qquad \text{............ (xxii)}$$

$$\Delta P = \frac{\Delta E_{fe} + \Delta E_{fs}}{\Delta\bar{\delta}} \qquad\qquad\qquad \text{............ (xxiii)}$$

$$\Delta E_{fe} = 2P_m\mu_e\Delta\bar{u}_e \qquad\qquad\qquad \text{............ (xxiv)}$$

$$\Delta E_{fs} = I(J - 1)P_m \cos\emptyset'\, \mu_s\Delta\bar{u}_s \qquad\qquad \text{............ (xxv)}$$

Here, E_{fe} & E_{fs} are the frictional dissipation due to edge friction and surface friction respectively. The sum of these two components divided by the equivalent displacement gives the value of frictional load, which ultimately alters the master curve (P_m).

The notation $\emptyset'$ in above equation is different from the angle $\emptyset$ which was defined earlier. $\emptyset'$ is the measure of instantaneous spring angle measured between spring and the horizontal and can be calculated from interpolation method as a function of spring deflection(δ).

Table 5: Interpolation table for intermediate spring angle, Ø'

	Initial point	Final point	Intermediate points
Deflection	0	$h = H - t\cos\emptyset$	δ
Spring angle ($\emptyset'$)	$\emptyset$	0	$\emptyset \times \left(1 - \dfrac{\delta}{H - t\cos\emptyset}\right)$

It can be observed from the equations that equivalent displacement ($\bar{\delta}$) is used to calculate the Almen-Laszlo's load approximation and frictional losses instead of total deflection (δ), where equivalent displacement ($\bar{\delta}$) is the displacement per series stack. This is because when Belleville springs are stacked together, I number of springs in series multiplies the total deflection by I and J number of springs in parallel multiples the total load by J [19]. Thus, when the total deflection of the spring stack is δ, deflection of each series stack will be $\bar{\delta} = \delta/I$.

So far, the methodology to calculate the displacement of different points of spring during deflection has been derived via interpolation method. Next, the relation for frictional dissipation as proposed by Ozaki et. al. [23] is implemented and the modified load-deflection curve is generated. Figure 40 shows a load-deflection curve obtained from above interpolation method for the spring parameter $H = 1.7$, $r_1 = 18.08$, $r_2 = 24.45$, $t = 0.5$, $I = 3$, $J = 2$. In the graph, the solid line represents frictionless sceanario while the broken lines represent combinations of different values of edge and surface friction coefficient. It can be observed from the graph that the more the friction coefficient, the more is the deviation of the load-deflection curves from the frictionless curve. Furthermore, the force needed to compress the spring increases and the force dissipated by the spring relaxation reduces due to friction.
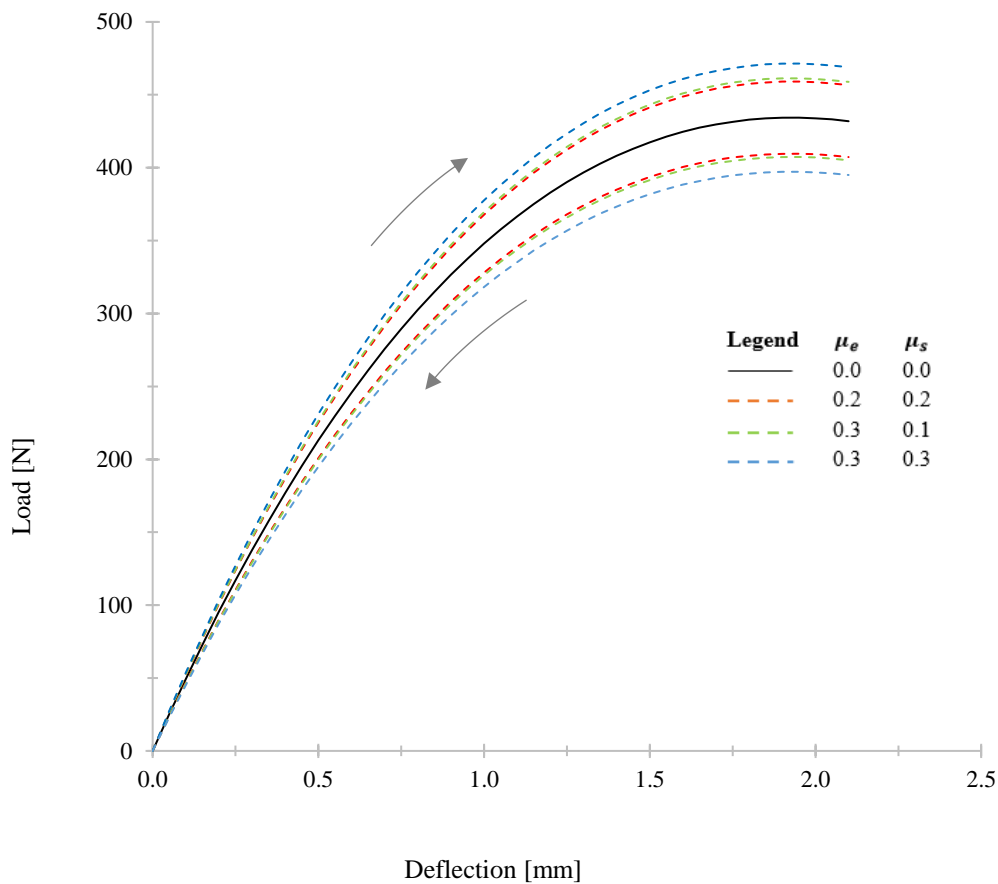
Figure 40: Load-deflection curve generated by proposed method
[Spring parameters (mm): H = 1.7, r₁ = 18.08, r₂ = 24.45, t = 0.5, I = 3, J = 2]

5.5.1. Effect of Free height to Thickness ratio

Next, the effect of spring parameters on frictional loss in Belleville springs is studied. One of the parameters used in specifying the Belleville springs is free height to thickness, h/t ratio. A set of h/t ratios [0.5, 1, 1.4 and 2.4] were plotted for the $I = 2$, $J = 2$ spring configuration with constant edge friction coefficient ($\mu_e = 0.3$), and varying surface friction coefficient ($\mu_s = 0, 0.1, 0.3$).

Different sets of h/t ratios were obtained by keeping total height of the spring constant at $H = 1.7\,mm$ and changing the thickness, t. Figure 40 is the graph obtained by plotting the load-deformation diagram of these spring configuration, which is identical to the one plotted by Ozaki et. al [6, Figure 10 a].

Figure 41: Effect of change of h/t ratio on frictional dissipation
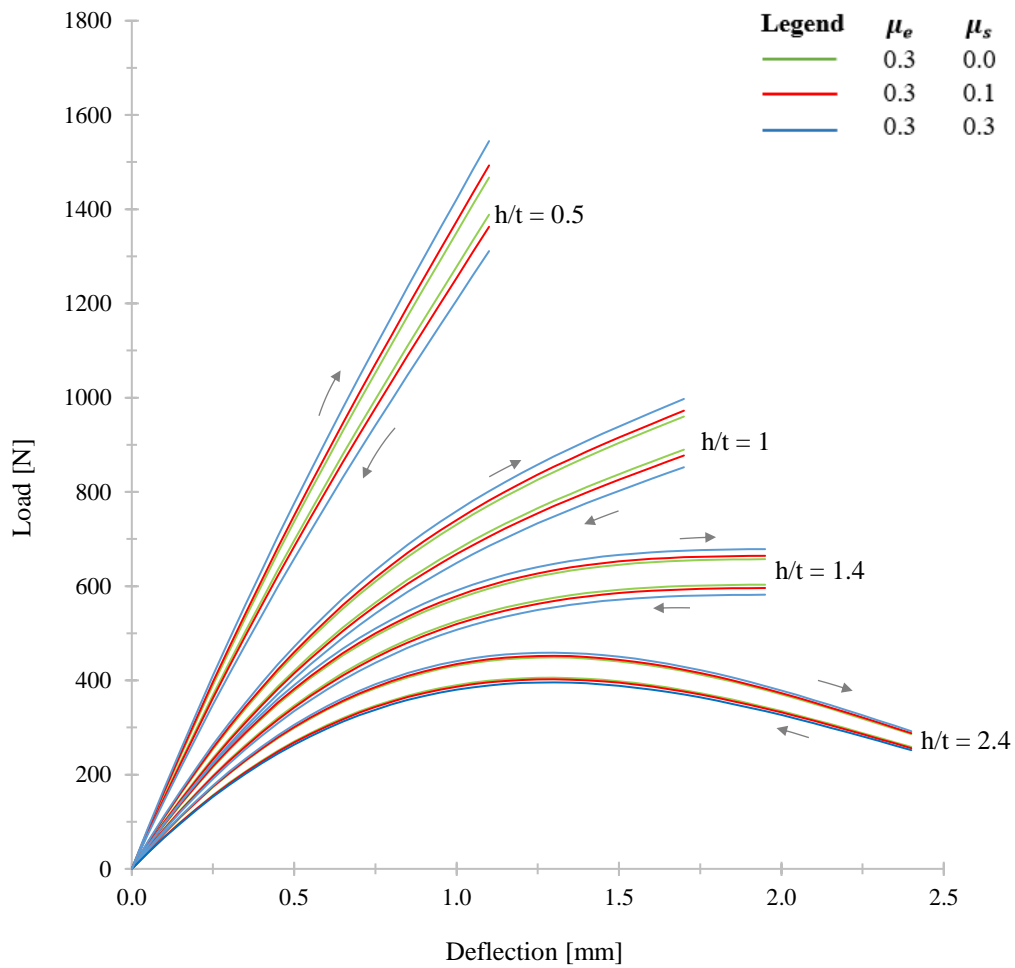*[Spring parameters (mm): H = 1.7, r₁ = 18.08, r₂ = 24.45, I = 2, J = 2]*

Figure 41 can also be used to identify the type of Belleville spring by the nature of its load-deflection curve. As grouped by most of the manufacturers, Belleville springs can be categorized into High Load, Standard, Force Limiting and Force Adjusting Belleville springs [18]. The springs that produce curves similar to $h/t = 0.5$ can be categorized as High Load Belleville springs. These springs are very thick and have high load capacity. The load-deflection curve for these springs is mostly linear. Similarly, springs with curves similar to $h/t = 1$ are the Standard Belleville springs; these springs are known for their excellent fatigue resistance. Load-deflection curve of the Standard Belleville springs are linear for small deflections. The third type of spring that can be identified by the load-deflection curve corresponds to $h/t = 1.4$, Force Limiting Belleville springs. The load-deflection curve for these types of springs is linear when the spring starts to deflect and becomes flat after certain amount of compression. Because of this nature, these types of springs are used in clutches, brakes or PSVs. The fourth category of Belleville spring is the Force Adjusting type. These springs have high h/t ratios, 2.4 in this case. The load-deflection curve for these springs starts out linear, reaches a maximum value and then loses force after certain percentage of deflection.

5.5.2. Effect of Diameter ratio

The effect of diameter ratio, γ on the load-deflection curve can be observed in the similar manner. For this, three diameter ratios $[\gamma = 1.4, 1.6 \text{ and } 2]$ were plotted for a spring with $r_2 = 24.45 \text{ mm}, t = 0.5 \text{ mm and } H = 1.7 \text{ mm}$. The value of r_1 was varied to match the corresponding diameter ratio. Figure 42 shows the curves plotted with these scenarios together with the variation in friction coefficients. It is observed that, as the diameter ratio increases, springs

become less stiff. Moreover, the effect of friction is seen to be identical in all configurations. The illustrated graph represents a Force Adjusting Belleville spring with h/t ratio of 2.4. It is seen that altering the diameter ratio does not have much effect in the nature of the load-deflection curve; rather it shifts the peak of the load-deflection curve.
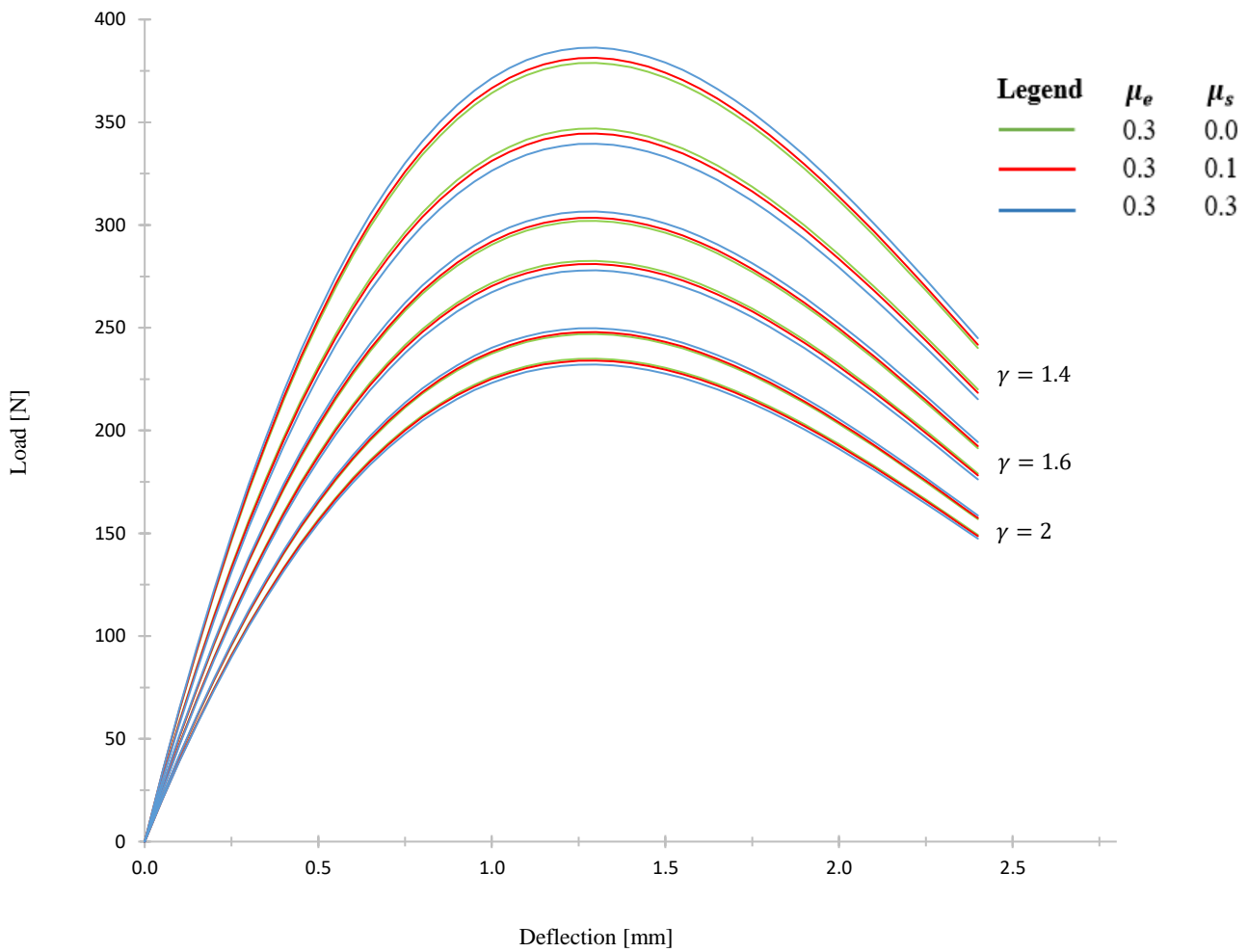

Figure 42: Effect of change of diameter ratio on frictional dissipation
[Spring parameters (mm): H = 1.7, r_2 = 24.45, t=0.5, I = 2, J = 2]

5.6. Analysis of Load-deflection curves of LSD p-VARD Springs

In this section, we use the methodology that has been developed to analyze the Belleville springs used in LDS p-VARD tool. This requires the understanding of the load-deflection curves of the Belleville springs, with and without the effects of friction. Specifications of the springs that are analyzed is listed in Table 6.

Figure 43 shows the load-deflection curves for the $I = 2$, $J = 2$ configuration of all four springs with constant edge friction coefficient ($\mu_e = 0.3$), and varying surface friction coefficient ($\mu_s = 0$ & 0.3). The graph of this nature helps visualize how spring deflection is going to vary with varying load, which in the case of p-VARD tool is the WOB.

The characteristics curves of Figure 43 illustrates the nature of spring stiffness exhibited by the LDS p-VARD Belleville springs. Spring #1 with $h/t = 1.0$ exhibit the characteristics of a Standard Belleville spring i.e. the deflection is proportional to load at the beginning of the stroke only. As the load increases further, the curve tends to become more cubical in nature. Because of this nature of spring #1, when configuring the p-VARD tool with this spring, one should be careful not to approach the full stroke of the spring compression. Similarly, spring #2 with $h/t = 0.62$ appears to have more linear load-deflection relationship than spring #1. Spring #3 and #4 on the other hand have fully linear load-deflection relationship.

The other goal of the analysis is to understand the nature of frictional losses in Belleville springs of the p-VARD tool. From the graphs that have been plotted, it is observed that frictional loss is directly proportional to compressive force. Moreover, surface friction accounts for higher losses

than the edge friction as soon as the number of parallel stacking is increased to $J = 2$. This phenomenon is observed in all four springs.
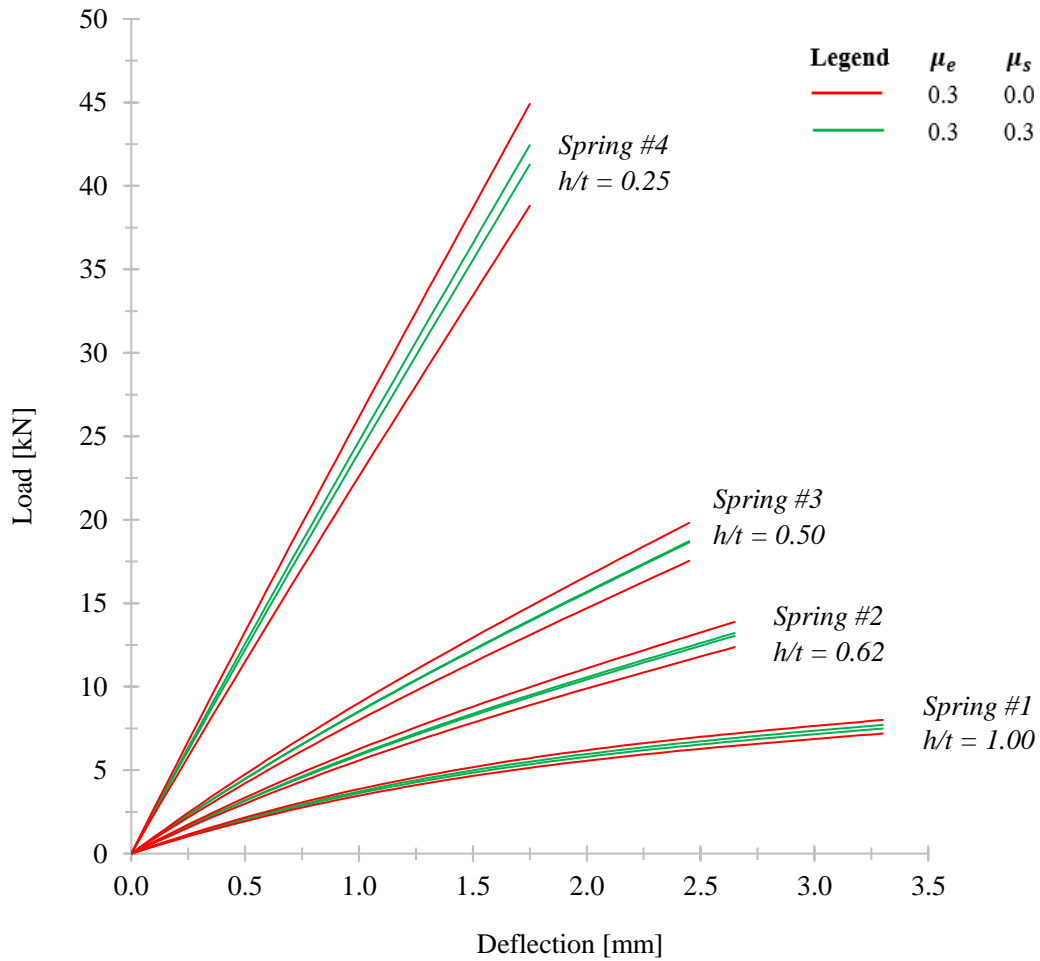

Figure 43: Load-deflection diagram of Belleville springs for LDS p-VARD
[System parameters: I=1, J=2]

5.7. Discussion and Conclusion

In this chapter, a method of interpolation has been used to calculate the frictional losses in Belleville springs. This method relies on the basis assumptions put forth by Almen-Laszlo in their original work [13] and on the modification of the work by Ozaki et. al. [23], which was based on the method of rotational matrix. Observation of the results plotted by this method reveals some interesting facts about the characteristics of these springs.

Frictional losses in the springs is dependent on type of spring stacking. When the number of springs stacked in parallel is less, edge friction accounts for most of the frictional loss. This does not hold true when the number of parallel springs is increased, where surface friction becomes more dominant. This key feature can be used in designing the spring stacks with calibrated frictional loss or to calculate the frictional losses of the installed equipment.

Similarly, different types of Belleville springs exhibit different nature of frictional dissipation. For the High Load and Standard Belleville springs, frictional loss increases with increase in spring deflection. However, for the Force Limiting Belleville springs, frictional loss becomes constant at the flat region of the load-deflection curve and for the Force Adjusting Belleville springs, frictional loss is maximum at the peak of load-deflection curve and starts to decrease as the spring is compressed more. Regardless of type of spring, a common dependence of frictional loss on the compressive force is observed in all kinds of springs. This is because frictional loss is a function of reaction force generated by the compressive force. So, the more the spring is compressed, the more is the friction generated.

It is also observed from the graphs that maximum load of these springs varies as per the type of spring or more parametrically, on the h/t ratio. More predominantly observed in the Force Limiting and Force Adjusting springs, increasing the load beyond the maximum load causes the springs to lose force or provide steady resistance to deformation. Understanding the characteristic curve and the hysteresis loop of Belleville springs is crucial while designing components involving these springs as selection of spring with inadequate capacity may lead to unsatisfactory performance of the component and/or its failure.

This approach of calculating the frictional losses can be experimentally validated. Based on the theoretical understanding of this phenomenon, it can be predicted that the experimental curve for spring compression will to be similar to the loading curve presented in Figure 40. Variation of the experimental results from this theory, if any, can be used in calibrating this model to improve or validate its accuracy. As far as the nature of the load-deflection curve is concerned, changing the spring configuration only scales up/down the values of maximum load and/or maximum deflection while maintaining the original characteristics of a single spring.

The methodology developed in this chapter is implemented in Section 5.6 to plot the load-deflection curves of the springs used in LDS p-VARD tool. It can be concluded that predicting the spring behaviours is indeed critical as some springs like Force Limiting and Force Adjusting Belleville springs may lose the force as the spring deflection increases.

Chapter 6   Design and Analysis of p-VARD tool for LDS

6.1. Introduction

The use of p-VARD tool has been introduced with the intend of increasing the drilling rate of penetration, without increasing the parameters like WOB, rpm and torque. Researchers have performed multiple experiments, field trials and simulations to examine the effects of using a p-VARD tool, and produced some promising results. However, all the experimental works involving a p-VARD tool have been performed in the Small Drilling Simulator (SDS) only. Although SDS has a wide operational range, it only has two rotary speeds (300 rpm and 600 rpm) and its suspended weight system is not smooth. Furthermore, the axial movement of its drill string is not instrumented and requires a visual reading of the scale to know the drilling depth.

On the other hand, Large Drilling Simulator is more sophisticated and highly instrumented. It can perform drilling experiments at any speeds between 1 rpm and 1000 rpm and apply a maximum torque of 1200 Nm. The WOB is applied through the pneumatic cylinders and the operator can choose any WOB between 0 to 100 kN. In this chapter, a p-VARD tool has been designed to be operated in the LDS. The tool is designed to withstand the maximum forces delivered by the LDS with a minimum safety factor of 3.4. In addition to this, the characteristic curves of the Belleville springs used in the LDS p-VARD is plotted with the method developed in Chapter 5.

6.2. Design of LDS p-VARD

This section of the thesis summarizes basic characteristic of different components that make up the LDS p-VARD tool. There are four 5 major components of the LDS p-VARD tool; 1) Inner shaft, 2) Outer shell, 3) Keys, 4) Sensor plate, 5) Belleville Springs and Rubbers. These parts are explained in more detail in following sections:

6.2.1.   Inner Shaft

The top of the Inner shaft is designed to connect to the existing swivel of the LDS such that it receives the torque and WOB from the LDS. The torque is transmitted to the Outer shell of the p-VARD through the keys, which are located 90º apart on its circumference. Similarly, the WOB is transmitted to the Outer shell through the stack of Belleville springs. The Inner shaft also has a 13 mm through hole for the purpose of fluid circulation. One of the important feature that the Inner shaft houses is the grooves of the O-rings, which are designed to seal the spring lubricants. The key features of the Inner shaft of the LDS p-VARD, are highlighted in Figure 44.

6.2.2.   Outer shell

The Outer shell of the p-VARD acts like a cover for the inside p-VARD components like the spring and the rubber and also seals against the O-rings to prevent any leakage of the spring lubricants. The slots for the keys are cut on the circumference of the Outer shell and are made such that it still allows an axial movement of 32 mm to allow for the compression of the springs. The bottom of this shell connects to the rest of the drill string of the LDS. In addition, the top of the Outer shell has a 5 mm turning for placing the sensor plate. In the inside, the outer shell has different diameters,

which allow the compression of springs and rubbers. These features of the Outer shell are illustrated in Figure 45.
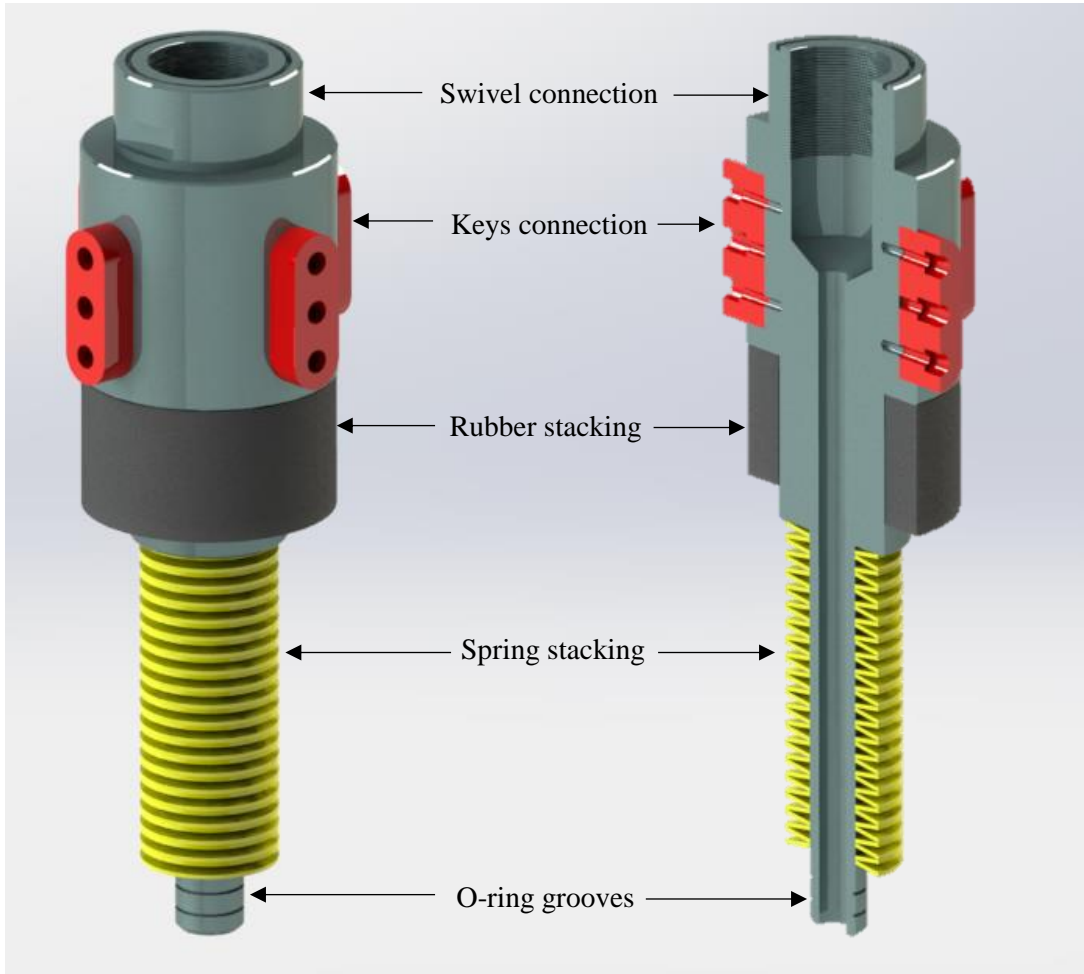
6.2.3. Keys

There are four Keys that transmit torque between the Inner and Outer shaft that are placed 90°
apart. One of the major features in the Keys are its three holes. Two of these holes in the top and

bottom don't have threads in them and are there to connect the keys to the Inner shaft. The middle hole is threaded and its purpose is to pop out the keys from the Inner shaft while disassembling (Refer to Figure 44 for more details). All three holes are designed for the M5 × 1 screws.
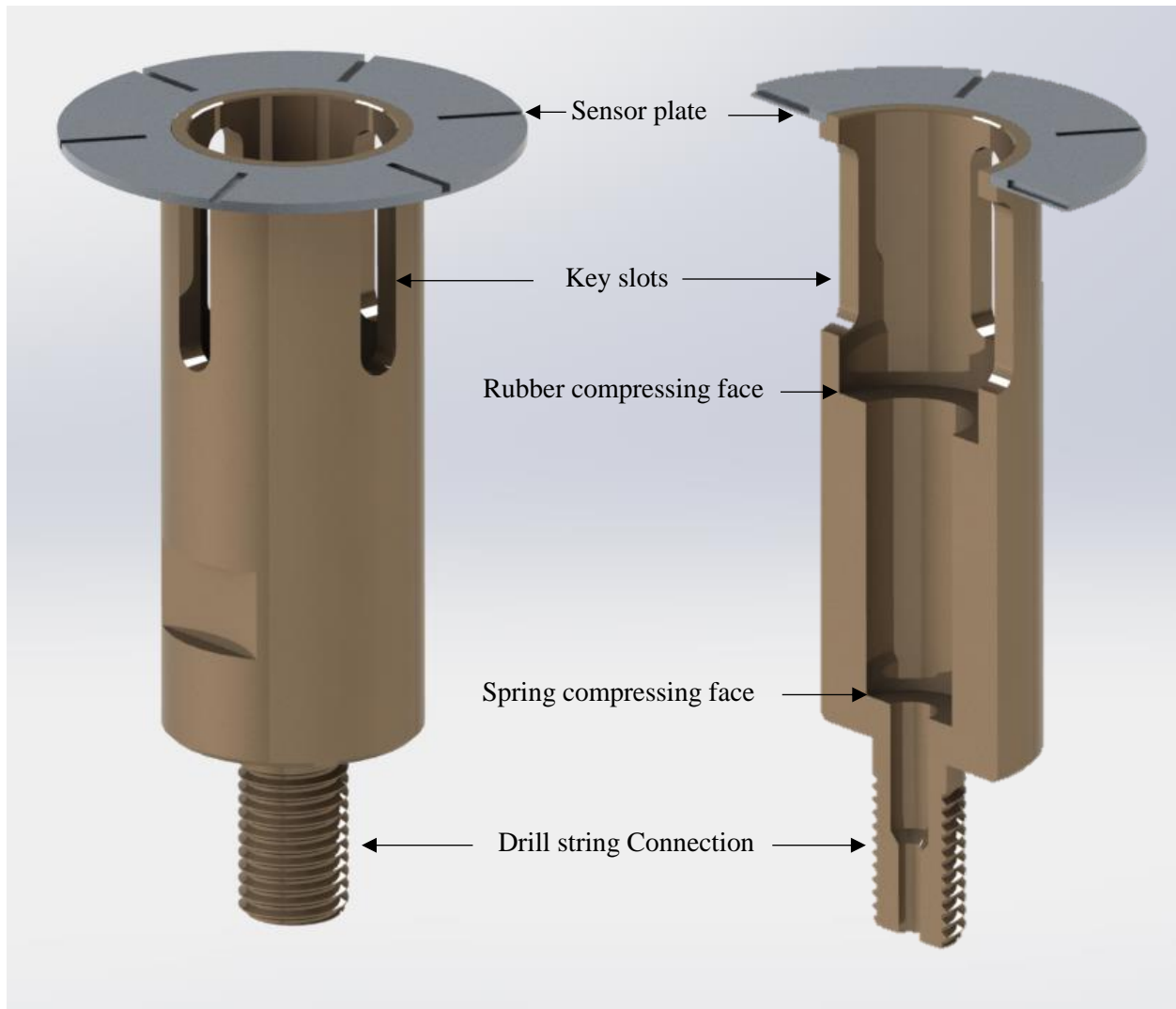

Figure 45: Showing different parts of p-VARD outer shell

6.2.4. Sensor plate

The sensor plates is made up of 5 mm thick aluminium with 6 uniformly spaced grooves. Five grooves have the cross-section of 5 mm (width) × 3.5 mm (depth) and one groove has the cross-section of 5 mm (width) × 1.5 mm (depth). The unique depth of one of the grooves is to identify completion of one rotation during data analysis. The details on location and assembly of this component can be referred from Figure 45.

6.2.5. Belleville Springs and Dampers

The LDS p-VARD is designed for the Belleville Springs with 1 inch ID and 2 inch OD. The rationale behind the selection of this particular dimension of the Belleville springs is the availability of 4 different springs with unique compliances that share the same dimensions (ID and OD). This makes it easy to change the compliance of the tool itself not only by changing the spring configuration but also by using a different spring. This increases the range of working load of the p-VARD tool. Table 6 gives the detail dimensions of all four of these springs. The height of the spring stack is designed to be 5 inches, in an experimental scenario where total spring height is less than 5 inches; the remaining space should be filled with rigid spacers to make up for the insufficient height.

Likewise, the damping unit is made up of series stack of 2.35 inch ID and 3.70 inch OD neoprene rubbers, each 0.25 inch thick. The total height of the rubbers is designed to be 2 inches, while assembling the tool.

Spring number	ID d_1 (in)	OD d_2 (in)	Thickness t (in)	Total height H (in)	h/t
1	1	2	0.065	0.13	1.00
2	1	2	0.084	0.136	0.62
3	1	2	0.097	0.145	0.50
4	1	2	0.142	0.177	0.25

6.3. FEA Analysis of the LDS p-VARD

The Finite Element Analysis of the LDS p-VARD is performed to determine the high stress concentration points and to optimize the design accordingly. From the preliminary study, the most vulnerable area of the p-VARD is identified as the torque transmitting unit, which comprises of the keys, outer shell and the inner shaft. A simplified model of the p-VARD tool is used to perform the FEA analysis as shown in Figure 46, where the complex features like thread, chamfers, through holes (in the Inner shaft), etc. of the components are supressed.
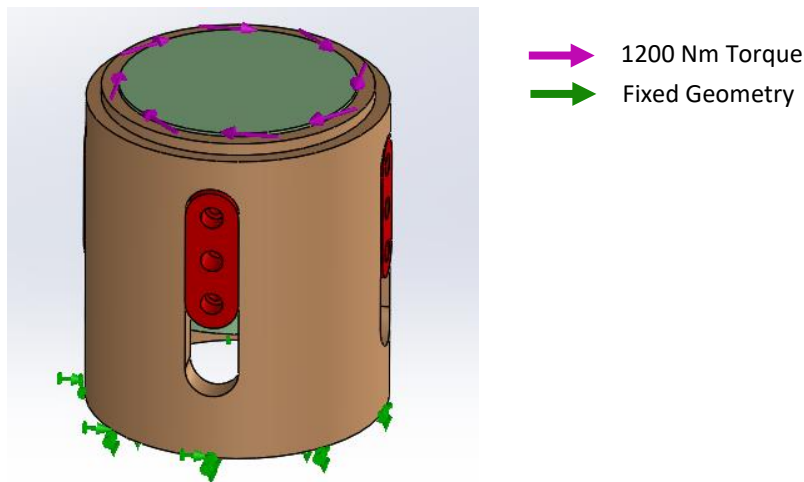

1200 Nm Torque
Fixed Geometry

Figure 46: FEA Model for the p-VARD

The top drive system of the LDS runs on a synchronous torque motor S.N. *DST2-135YO54W-035-5* with maximum cold motor torque of 1,200 Nm, which decreases with increase in operating temperature and the speed [42]. Hence, for the purpose of the simulation, the lower face of the outer shell is fixed and a torque of 1,200 Nm is applied to the top of the inner shaft. This number for the torque comes from the characteristics curve of the top drive motor of the LDS, which is shown in Figure 47.
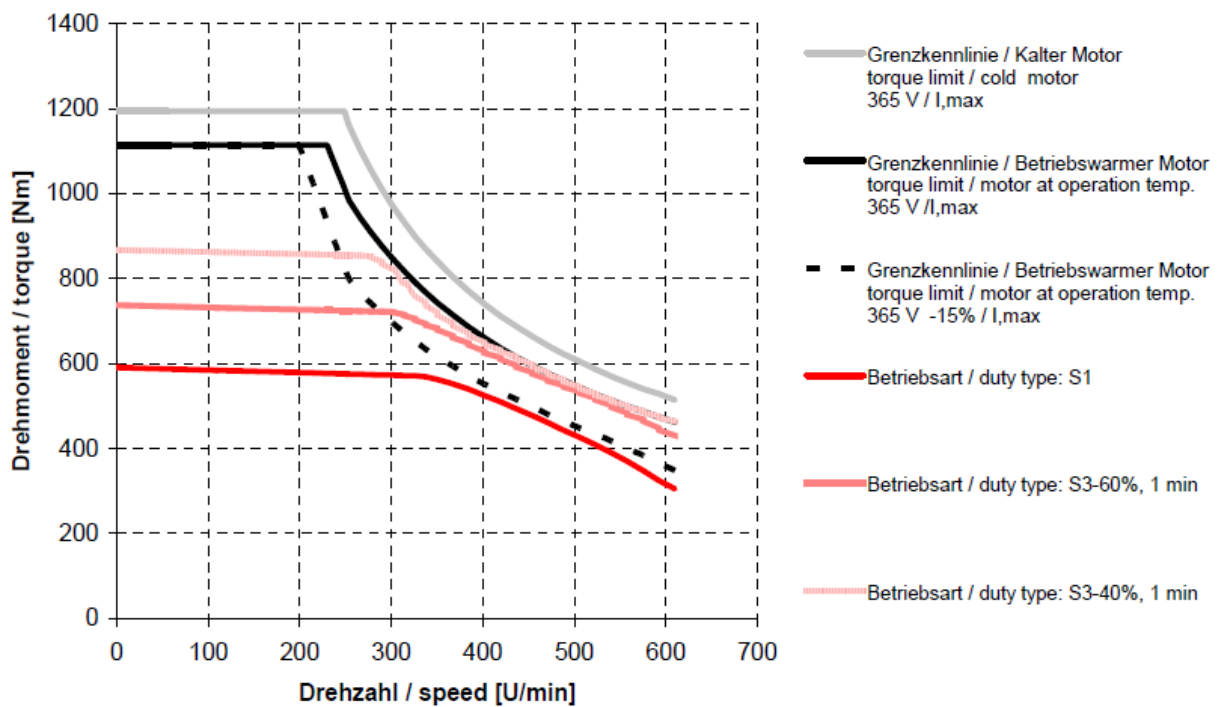

Figure 47: LDS TDS Motor characteristics curve, S. N. DST2-135YO54W-035-5 [42]

The FEA analysis of the p-VARD tool is performed in SolidWorks using curvature-based mesh, which automatically creates more elements in higher-curvature areas without the need of mesh control. Similarly, high quality second order tetrahedral element defined by four corner nodes, six mid-side nodes and six edges is selected. These elements increase the accuracy in exchange for more computational time. To verify the convergence of the FEA model, the global mesh size is gradually reduced and the corresponding simulation parameters along with maximum von Mises stress is recorded. These data points are used to plot the mesh convergence plot shown in Figure 48.
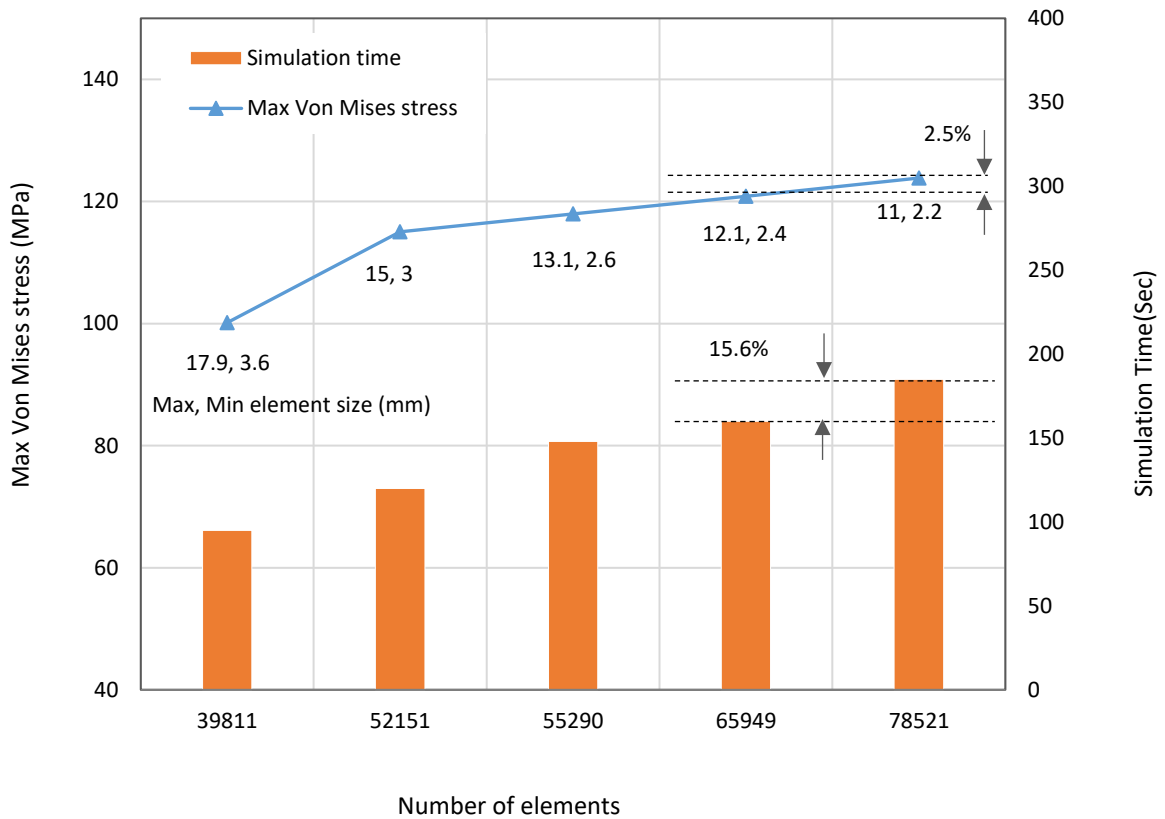

Figure 48: Mesh convergence plot

It is observed from the plot that the final simulation yields 2.5% increase in the maximum stress at the expense of 15.6% raise in the computational time. Therefore, for the purpose of this simulation, this iteration is skipped, and the curvature based mesh with global mesh size of 12.1 mm is selected with 65,949 number of elements.

The below table summarizes the configurations of the FEA.

Table 7: Summary of configuration settings for FEA

Particular	Description
Components	Keys, Inner shaft & Outer shell
Material	AISI 4140 Steel
Tensile Strength (σ_t)	655 MPa
Yield Strength (Y_s)	415 MPa
Young's Modulus (E)	200 GPa
Meshing	Curvature-based mesh
Mesh quality	High
Mesh Type	Second order tetrahedral
Minimum element size	2.4 mm
Maximum element size	12.1 mm
Number of elements	65,949
External Load	
Torque	1200 Nm

6.4. Simulation Results

The results from the simulation show that the maximum stress is observed in the inside curves of the outer shell that touches the keys (refer to Figure 49). The maximum von Mises stress is compared to the material Yield strength to observe the factor of safety (FOS) of the assembly,

where FOS is defined as the ratio of Yield strength to von Mises stress. Figure 50 shows the minimum FOS (3.4), which corresponds to the maximum stress of the assembly.
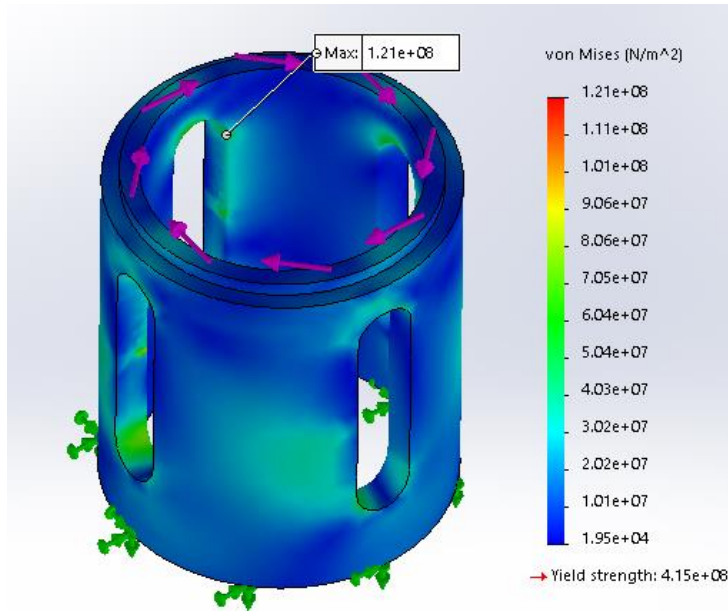

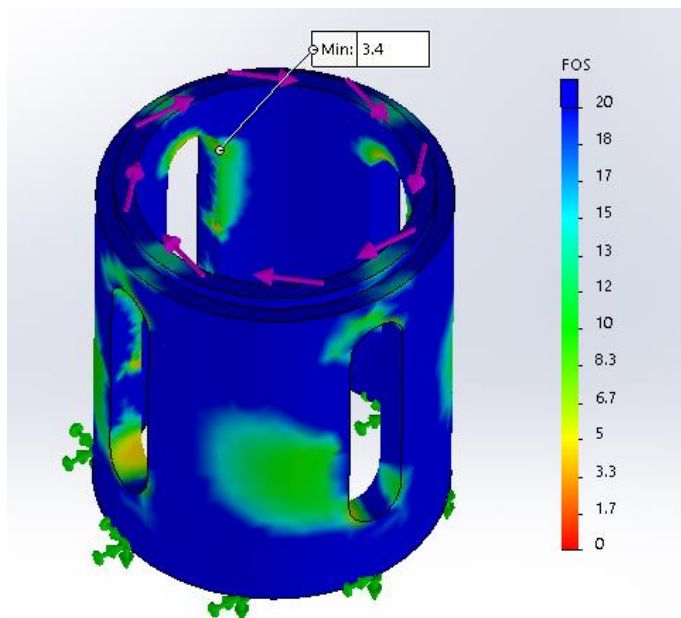*Figure 49: Showing maximum von Mises stress*

Figure 50: Showing minimum FOS of the assembly

6.5. Discussion and Conclusion

The results from the simulation show that the p-VARD tool fulfills the safety requirement with minimum FOS of 3.4. The practical FOS of the tool will be even higher because in the real case scenario, the maximum torque of 1,200 Nm will not be reached. This is because the rotation of the drill string and the rise in the motor temperature will lower the motor torque thus increasing the tool safety factor. However, the operator should be careful not to compress the springs more than 32 mm, which is the design limit of the tool. The scope of this work is limited to the design and static analysis of the p-VARD tool for the LDS. It does not include the tasks related to the fatigue analysis, design of experiment, and calibration of the tool compliance. A dynamic analysis of this tool can give us more information on these topics, which can be performed as a future research.

Chapter 7   Conclusion and Recommendations

This chapter is comprised of the concluding remarks from the three main tasks reported in this thesis. In Chapter 4, the rigid and compliant drilling modes of Small Drilling Simulator of the Drilling Technology Laboratory, MUN is analyzed with bond graphs. It is observed that the resonating frequency of the compliant drilling system is significantly lowered by the use of p-VARD tool, which would allow resonance to take place at a lower frequency. This sort of dynamic analysis of the drill string with the p-VARD tool helps in identifying the combination of vibration frequency and amplitude which could result in unwanted flattening of the springs. A driller can then use these data to effectively plan the drilling experiments/field works. One of the bases that the use of p-VARD tool can be contested is that, operating a drill string at its resonating frequencies is not recommended as per the best practices in drilling engineering as it results in premature failure and shortening of the fatigue life. However, this study issue needs to be further analyzed through experiments and numerical simulations, which will be able to interpret these effects quantitatively or qualitatively.

In Chapter 5 frictional losses in Belleville springs have been modelled by studying the movement of the springs in series and parallel stacking. At first, the starting and the ending points of the spring movement are calculated in terms of spring parameters. After that, linear interpolation is used to calculate the intermediate positions of these points, which is then used to calculate the frictional dissipation in each spring cycle. The hysteresis model that is developed, is used to study the frictional losses in different kinds of springs and determine its relation with respect to different

spring parameters. This model is also used in Section 5.6 to analyse the nature of frictional losses in four different LDS p-VARD springs and understand their load-deflection relations.

Finally, a finite element analysis of a LDS p-VARD tool has been presented in Chapter 6. Results from the FEA analysis show that the tool has a minimum FOS of 3.4. Although this FEA analysis only deals with static analysis of the tool, results from the dynamic analysis in Chapter 4 show that the p-VARD tool can be compressed beyond its static deflection when it is excited near its natural frequency, regardless of the excitation amplitude. To prevent this, the experiments should be simulated before performing them in the lab, which will avoid the unwanted frequency ranges. This will prevent the unwanted flattening of springs or compressing it beyond tool design limit. Similarly, it is also observed that the damping material has significant effect in minimizing the tool vibration. Future work involving p-VARD tool should study the effect of using different settings of the damping material to characterize its effects. As a further step to calibrate the p-VARD tool, the p-VARD index can be developed to readily make available the optimal tool settings that that will produce the best results in drilling experiments. This will require a series of numerical simulation and experiments and are the future scope of works.

Reference

[1]   M. Kapitaniak, V. V. Hamaneh, J. Páez Chávez, K. Nandakumar, and M. Wiercigroch, "Unveiling complexity of drill-string vibrations: Experiments and modelling," 2015.

[2]   B. Cayres, C. Fonseca, A. Santos, and H. I. Weber, "Analysis of Dry Friction-Induced Stick-Slip in an Experimental Test Rig Modeling a Drill String," *Mech. Mach. Sci.*, vol. 21, 2015.

[3]   Y. Liu, W. Lin, J. Páez Chávez, and R. De Sa, "Torsional stick-slip vibrations and multistability in drill-strings," *Appl. Math. Model.*, vol. 76, pp. 545–557, Dec. 2019.

[4]   R. Rahman, "Development and Interpretation of Downhole Data from Downhole Vibration Monitoring Tool," Memorial University of Newfoundland, 2015.

[5]   G. P. G. Sotomayor, J. C. Placido, and J. C. Cunha, "Drill String Vibration: How to Identify and Suppress," in *Fifth Latin American and Caribbean Pertoleum Engineering Conference*, 1997.

[6]   P. D. Spanos, A. K. Sengupta, R. A. Cunningham, and P. R. Paslay, "Modeling of Roller Cone Bit Lift-off Dynamics in Rotary Drilling," *J. Energy Resour. Technol. Trans. ASME*, vol. 117, pp. 197–207, 1995.

[7]   P. C. Kriesels, W. J. G. Keultjes, P. Dumont, I. Huneidi, O. O. Owoeye, and R. A. Hartmann, "Cost Savings through an Integrated Approach to Drillstring Vibration Control," pp. 1–12, 1999.

[8]   D. K. Ashley, X. M. McNary, and J. C. Tomlinson, "Extending BHA life with multi-axis vibration measurements," *Proc. Drill. Conf.*, vol. 1, pp. 89–99, 2001.

[9]   W. Borutzky, *Bond graph methodology: Development and analysis of multidisciplinary dynamic system models*. Springer London, 2010.

[10]   D. Karnopp, "Analog techniques for representing mechanical dissipation," vol. 6, no. 3, pp. 149–151, 1966.

[11]   D. C. Karnopp, D. L. Margolis, and R. C. Rosenberg, *System Dynamics*, 5th ed. John Wiley & Sons, Inc., 2017.

[12]   R. L. Nailen, "When , and how , to use Belleville washers," *Electr. Appar.*, pp. 21–26.

[13]   J. O. Almen and A. Laszlo, "The uniform-section disk spring," *Trans. Am. Soc. Mech. Eng.*, vol. 58, pp. 305–314, 1936.

[14]   Y. Zhiming and Y. Kaiyuan, "A study of belleville spring and diaphragm spring in engineering," *J. Appl. Mech. Trans. ASME*, vol. 57, no. 4, pp. 1026–1031, 1990.

[15]   G. La Rosa, M. Messina, and A. Risitano, "Stiffness of variable thickness belleville springs," *J. Mech. Des. Trans. ASME*, vol. 123, no. 2, pp. 294–299, 2001.

[16]   Ş. Karakaya, "Investigation of hybrid and different cross-section composite disc springs using finite element method," *Trans. Can. Soc. Mech. Eng.*, vol. 36, no. 4, pp. 399–412, 2012.

[17] G. Curti and R. Montanini, "On the influence of friction in the calculation of conical disk springs," *J. Mech. Des. Trans. ASME*, vol. 121, no. 4, pp. 622–627, 1999.

[18] "Belleville International >» Load vs. Deflection." [Online]. Available: https://bellevilleintl.com/engineering/load-vs-deflection/. [Accessed: 15-Jun-2020].

[19] M. Paredes and A. Daidié, "Optimal catalogue selection and custom design of belleville spring arrangements," *Int. J. Interact. Des. Manuf.*, vol. 4, no. 1, pp. 51–59, 2010.

[20] C. W. Coffman, "Progressive gun spring recoil system with high energy rebound," 15-Oct-2013.

[21] "Disc Springs in the Automotive Industry | Mubea Disc Springs." [Online]. Available: https://mubea-discsprings.com/disc-spring-applications/automatic-transmission/. [Accessed: 16-Jun-2020].

[22] "Automatic Tool Clamping System TGSP." [Online]. Available: https://www.ortlieb.net/en/1/tool-clamping/automatic-tool-clamping-system-tgsp/. [Accessed: 16-Jun-2020].

[23] S. Ozaki, K. Tsuda, and J. Tominaga, "Analyses of static and dynamic behavior of coned disk springs: Effects of friction boundaries," *Thin-Walled Struct.*, vol. 59, no. January, pp. 132–143, 2012.

[24] P. S. Rana, A. N. Abugharara, J. Molgaard, and S. D. Butt, "Experimental Evaluation of passive-Vibration Assisted Rotary Drilling (p-VARD) tool to Enhance Drilling

Performance," *49th US Rock Mech. / Geomech. Symp. 2015*, vol. 3, pp. 1729–1734, 2015.

[25] B. G. Gillis and S. D. Butt, "Comparison of field and laboratory vibration assisted rotary drilling," *52nd U.S. Rock Mech. Symp.*, 2018.

[26] A. Alwaar, A. N. Abugharara, and S. D. Butt, "PFC-2D numerical study of the influence of passive vibration assisted rotary drilling tool (pVARD) on drilling performance enhancement," *Proc. Int. Conf. Offshore Mech. Arct. Eng. - OMAE*, vol. 8, pp. 1–9, 2018.

[27] S. Shah, Y. Xiao, S. Imtiaz, and S. D. Butt, "Investigation of Drilling Performance in Core Bit Drilling using passive Vibration-Assisted Rotational Drilling (pVARD) Technology," *72nd Can. Geotech. Soc. Annu. Conf.*, no. 2011, 2019.

[28] J. Molgaard, A. N. Abugharara, C. A. Hurich, and S. D. Butt, "Study of the influence of controlled axial oscillations of pvard on generating downhole dynamic wob and improving coring and drilling performance in shale," *Proc. Int. Conf. Offshore Mech. Arct. Eng. - OMAE*, vol. 8, pp. 1–7, 2019.

[29] W. C. Maurer, "The 'Perfect - Cleaning' Theory of Rotary Drilling," *J. Pet. Technol.*, vol. 14, no. 11, pp. 1270–1274, 1962.

[30] T. M. Warren, "Penetration-Rate Performance of Roller-Cone Bits.," *SPE Drill. Eng.*, vol. 2, no. 1, pp. 9–18, 1987.

[31] R. Teale, "The concept of specific energy in rock drilling," *Int. J. Rock Mech. Min. Sci.*, vol. 2, no. 1, pp. 57–73, 1965.

[32]   O. Oloruntobi and S. Butt, "Energy-based formation pressure prediction," *J. Pet. Sci. Eng.*, vol. 173, no. October 2018, pp. 955–964, 2019.

[33]   H. Li, S. Butt, K. Munaswamy, and F. Arvani, "Experimental investigation of bit vibration on rotary drilling penetration rate," *44th US Rock Mech. Symp. - 5th US/Canada Rock Mech. Symp.*, pp. 1–6, 2010.

[34]   Y. Babatunde, S. Butt, J. Molgaard, and F. Arvani, "Investigation of the effects of vibration frequency on rotary drilling penetration rate using diamond drag bit," *45th US Rock Mech. / Geomech. Symp.*, 2011.

[35]   M. Khademi, "Laboratory Study of the Effect of Axial Compliance on Rock Penetration of PDC Bits," Memorial University of Newfoundland, 2014.

[36]   H. Khorshidian, S. D. Butt, and F. Arvani, "Influence of high velocity jet on drilling performance of PDC bit under pressurized condition," *48th US Rock Mech. / Geomech. Symp. 2014*, vol. 1, pp. 343–348, 2014.

[37]   "Pipinato, A. (Ed.). (2016). Innovative bridge design handbook: Construction, rehabilitation and maintenance. Retrieved from https://ebookcentral-proquest-com.qe2a-proxy.mun.ca." .

[38]   "Belleville Disc Spring, for 3/4" Shaft Diameter, 0.755" ID, 1.5" OD, 0.0450" Thick | McMaster-Carr." [Online]. Available: https://www.mcmaster.com/9712K86. [Accessed: 16-Jun-2020].

[39]   J. Zhong, "Investigation of Bit-Rock Interaction for Rotary Drilling and Influence on

Penetration Rate," Memorial University of Newfoundland, 2015.

[40]   "'Detailed Vibration Isolation Theory - Farrat Resources,' Farrat. [Online]. Available: https://www.farrat.com/resources/detailed-vibration-isolation-theory. [Accessed: 09-Mar-2020].," 2016. .

[41]   F. Clayer, E. Aquitaine, J. K. Vandiver, and H. Y. Lee, "Effect of surface and downhole boundary conditions on the vibration of drillstrings," *Proc. - SPE Annu. Tech. Conf. Exhib.*, vol. Delta, pp. 431–442, 1990.

[42]   "DST2 high-torque motors: low-maintenance & energy efficient." [Online]. Available: https://www.baumueller.com/en/products/motors/high-torque-motors. [Accessed: 01-Jul-2020].